

OPEN ACCESS

EDITED BY

Alcione García-González, Universidad Autónoma de Nuevo León, Mexico

REVIEWED BY

Shila Neel,

Indian Council of Agricultural Research (ICAR), India

Erlintan Sinaga,

State University of Medan, Indonesia

Arief Wardani,

Universitas Muhammadiyah Magelang, Indonesia

*CORRESPONDENCE

Lei Yang,

☑ 156482281@qq.com

RECEIVED 21 May 2025 REVISED 06 October 2025 ACCEPTED 06 October 2025 PUBLISHED 11 November 2025

CITATION

Hao J, Li Q, Dong N, Zhou Y, Sun Y, Pei Y, Zhou X and Yang L (2025) Optimization of response surface methodology for the extraction of isoliquiritigenin from *Aspergillus niger* solid-state fermentation of licorice and its antitumor effects.

Front. Pharmacol. 16:1629167. doi: 10.3389/fphar.2025.1629167

COPYRIGHT

© 2025 Hao, Li, Dong, Zhou, Sun, Pei, Zhou and Yang. This is an open-access article distributed under the terms of the Creative Commons Attribution License (CC BY). The use, distribution or reproduction in other forums is permitted, provided the original author(s) and the copyright owner(s) are credited and that the original publication in this journal is cited, in accordance with accepted academic practice. No use, distribution or reproduction is permitted which does not comply with these terms.

Optimization of response surface methodology for the extraction of isoliquiritigenin from *Aspergillus niger* solid-state fermentation of licorice and its antitumor effects

Jingwei Hao¹, Qiuxuan Li¹, Nan Dong¹, Yi Zhou¹, Yifan Sun¹, Yingying Pei¹, Xiangkun Zhou¹ and Lei Yang²*

¹School of Life Science and Technology, Mudanjiang Normal University, Mudanjiang, China, ²Department of Pediatrics, The Second Affiliated Hospital of Mudanjiang Medical University, Mudanjiang, China

This research focused on optimizing the extraction of isoliquiritigenin (ISL) from licorice via a solid-state fermentation process involving Aspergillus niger. Isoliquiritigenin quantified through high-performance was chromatography (HPLC), initially assessed with one-way analysis and optimized using the Box-Behnken response surface method. The extracted isoliquiritigenin underwent structural modification, and the modified derivatives with enhanced activity were screened for in vivo antitumor efficacy using the MTT Colorimetric (MTT) assay. Finally, the structural and compositional alterations in the intestinal flora of the mice were evaluated post-administration of the extracted isoliquiritigenin. The results indicated that the optimal extraction conditions were pH 3.7, a solid-liquid ratio of 1:2, and an Aspergillus niger inoculum concentration of 1.5×10^6 , yielding 1.53 mg/g of isoliquiritigenin after fermentation for 4 days. This yield was 9 times greater than that obtained through conventional reflux extraction and 5.46 times higher than that from the ultrasonic extraction method. Nuclear Magnetic Resonance (NMR) analysis of isoliquiritigenin (ISL) and its derivatives revealed that the ISLb high dose group exhibited the most significant tumor suppression effect, with a suppression rate of 56.3%. In the mouse model following drug intervention, histopathological examination of kidney tissue via HE staining demonstrated that the safety profile of ISL-b was superior. Studies on the intestinal flora of mice revealed that the number of species was higher in the ISL-b high-dose group. Furthermore, there were significantly more species in the community samples than in the model group, with Micrococcus wartii accounting for the largest percentage at 24.49%. In the ISL-b dosing group, there was a significant increase in the abundance of Akkermansia muciniphila and Bradyrhizobium at the species level. The discoveries offer a robust scientific groundwork for developing antitumor drugs derived from isoliquiritigenin and enhance the broader application of licorice, a traditional herbal remedy.

KEYWORDS

licorice, isoliquiritigenin, solid-state fermentation of *Aspergillus niger*, antitumor, intestinal flora

1 Introduction

Glycyrrhiza uralensis Fisch, a perennial leguminous herb (Wang et al., 2021; Zhu et al., 2021), holds a significant position within the therapeutic framework of Traditional Chinese Medicine (TCM) (Cai et al., 2020; Yin et al., 2020). Its medicinal value is attributed to a diverse array of bioactive compounds (Nasiri et al., 2020; Ali et al., 2021), including flavonoids, polysaccharides, coumarins, inorganic elements, amino acids, organic acids, and triterpenoid saponins (Mohamad et al., 2018).

Isoliquiritigenin, a coumarin analog derived from licorice, exhibits significant antitumor activity (Chen et al., 2021; Ting and Chen, 2022). It exerts anticancer effects by inhibiting the NF-κB pathway, inducing apoptosis in cancer cells, blocking the PI3K/AKT signaling pathway, and activating ROS-mediated oxidative damage (Yu et al., 2018; Lin P.-H. et al., 2020). However, the traditional solvent extraction method is hindered by low yields (≤0.12%), the potential degradation of heatsensitive components, and environmental pollution (Das et al., 2022; Liang et al., 2022), which severely restricts its medicinal development. In this context, microbial solid-state fermentation technology, known for its efficient biocatalysis, environmental sustainability, and product stability, has emerged as an ideal solution to overcome the bottlenecks in the industrial production of natural products (Xin et al., 2014; Wu et al., 2021). This study provides an example for the "development of microbe-derived bioactive components" in the field of natural product extraction; in the field of microbial metabolism, it lays a foundation for the subsequent investigation into the metabolic pathway of isoliquiritigenin synthesis by Aspergillus niger and facilitates research on microbial metabolic regulation.

Aspergillus niger, an engineered strain widely utilized in the production of secondary metabolites (Susca et al., 2016; Zhang et al., 2016), is a significant cellulase-producing organism (Schäpe et al., 2019; Lubna et al., 2022). It produces a comprehensive set of cellulose-degrading enzyme systems and is classified as a Generally Recognized As Safe (GRAS) strain. Its extracellular enzyme systems, including laccase and peroxidase, specifically degrade the cell wall of licorice to generate precursors of glycyrrhetinic acid, while simultaneously promoting the biosynthesis of isoglycyrrhetinic acid (Ji et al., 2022a; Wang Y. et al., 2022). However, the current fermentation process faces challenges such as significant pH fluctuations (ranging from 4.5 to 6.8) (Lima et al., 2019; Li M. et al., 2022), high temperature sensitivity (with an optimal temperature of 30 °C ± 2 °C) (Slivinski et al., 2011; Tao et al., 2022), and an imbalance in the carbon to nitrogen ratio (C/N ratio of 20-30), which leads to metabolite inhibition (Liang et al., 2021). Therefore, there is an urgent need to achieve breakthroughs in the process through a multi-objective optimization strategy.

Renal cell carcinoma (RCC) is one of the ten most common cancers worldwide and is the most prevalent type of kidney cancer (Park et al., 2020; Emaldi and Nunes-Xavier, 2022), originating from the epithelial cells of the renal tubules (Lin C.-L. et al., 2020; Kalantzakos et al., 2021). In recent years, the incidence of RCC has been steadily increasing (Scelo et al., 2018; Mittlmeier et al., 2022), with over 300,000 new diagnoses and more than 140,000 deaths attributed to this disease annually (Landberg

et al., 2019; Yan L. et al., 2021). As the second leading cause of cancer-related mortality globally (Swearson et al., 2022; Wang M. et al., 2022), the resistance to chemotherapeutic drugs and the severe toxic side effects associated with malignant tumors continue to pose significant challenges in clinical treatment (Chen et al., 2019; Qian et al., 2021).

Gut microbes and hosts form a "Holobiont" (symbiotic totality) (Jiang et al., 2022; Wong et al., 2022), and their symbiosis (De Bruijn et al., 2020; Li B. et al., 2022), co-metabolism, co-evolution, and coinfluence on host traits play important roles in regulating the host's nutrient absorption, energy metabolism, immune regulation, and behavioral patterns (Ji et al., 2022b). 16S rDNA is considered the most suitable indicator for phylogenetic and taxonomic identification of bacteria (Geng et al., 2022; Zhang et al., 2022), making it the preferred nucleic acid sequence for detecting species diversity. The imbalance of intestinal flora has been shown to be closely related to tumorigenesis (Meng et al., 2021; Xie et al., 2022), development, and drug response, suggesting its significant role in antitumor research (Wang et al., 2019). Although isoliquiritigenin has demonstrated antitumor potential, its low bioavailability, short half-life, and systemic toxicity have limited its clinical application (Kong et al., 2022; Shi et al., 2022).

Based on microbial solid-state fermentation technology, this study integrates response surface optimization and the MTT method to systematically investigate the inhibitory effects of drug delivery parameters on the growth of renal cancer cells. The aim is to enhance the yield of isoglycyrrhetinic acid glycoside and to analyze the conformational relationship between its structural modifications and antitumor activity. Through the observation of cell morphology and the assessment of growth and proliferation, the study reveals the direct effects of the drug on renal cancer cells. Additionally, it incorporates 16S rDNA sequencing analysis of intestinal flora to explore the dynamic changes in the intestinal microbial community under drug intervention, establishing a multidimensional research system encompassing the optimization of the fermentation process, assessment of tumor cell effects, and the correlation mechanism of intestinal flora. The scientific implications of this research framework are far-reaching: For the field of natural product extraction, it provides a paradigm for "microbial fermentation + response surface optimization" to improve the yield of bound-state active components (such as the isoliquiritigenin, ISL, in licorice), effectively addressing the bottlenecks of low yield and high environmental impact in traditional extraction methods and promoting the development of green and efficient extraction technologies; for microbial metabolism research, it clarifies the role of Aspergillus niger's enzyme systems (e.g., β-glucosidase) in the biotransformation of ISL (converting bound-state ISL to extractable free-state ISL), laying a solid foundation for subsequent studies on the regulation of microbial metabolic pathways related to natural product synthesis; for antitumor drug development, the screened highactivity derivative ISL-b exerts antitumor effects through dual mechanisms (direct inhibition of the NF-κB signaling pathway to induce cancer cell apoptosis + indirect regulation of intestinal flora to enhance beneficial bacteria such as Akkermansia muciniphila), offering a new target and theoretical reference for the design of natural product-derived antitumor drugs; for the modernization of Traditional Chinese Medicine (TCM), it breaks through the

conventional application boundaries of licorice (Glycyrrhiza uralensis Fisch), a classic TCM herb, and expands its medicinal value to the field of antitumor research. This framework is dedicated not only to the development of an efficient and low-consumption natural product extraction process but also aims to deepen scientific knowledge regarding the antitumor effects of isoliquiritigenin from the perspective of intestinal flora, while further providing robust theoretical and technical support for the industrialization of natural antitumor drugs.

2 Materials and methods

2.1 Materials and reagents

Experimental materials: identified as Uralic Glycyrrhiza uralensis Fisch, IsoGlycyrrhiza uralensis Fisch standard (HPLC≥98%, WM256.25, C15H12O4). Hepatocellular carcinoma cells HepG-2, lung cancer cells A549, renal clear carcinoma cells Caki-1, prostate cancer PC-3 cell lines, provided by Mudanjiang Medical College.

Main reagents: Chloro-1-butyl-3-methylimidazole (Beijing Kool Chemical Technology Co., Ltd., China), Bromo-1-butyl-3methylimidazole (Beijing Kool Chemical Technology Co., Ltd., China), 1-butyl-3-methylimidazole Hydrogen Sulfate (Beijing Kool Chemical Technology Co., Ltd., China), 1-butyl-3methylimidazole Nitrate (Beijing Kool Chemical Technology Co., Ltd., China), Anhydrous ethanol (Nanjing Xingsha Chemical Co., Ltd., China), methanol (chromatographically pure) (Fisher Chemical, United States), acetonitrile (chromatographically pure) (Fisher Chemical, United States), acetic acid (Tenda Chemical Reagent Factory, Dongli District, Tianjin, China), hydrochloric acid (Tenda Chemical Reagent Factory, Dongli District, Tianjin, China), sodium hydroxide (Tenda Chemical Reagent Factory, Dongli District, Tianjin, China), Agar powder (Beijing Aoboshin Biotechnology Co., Ltd., China), ultrapure water (Hangzhou Wahaha Group Co., Ltd., China), yeast powder (Beijing Aoboshin Biotechnology Co., Ltd., China), RPMI1640 medium (Gibco, United States), fetal calf serum (FCS) (Zheijiang Tianhang Bio-technology Co., Ltd., China), sodium bicarbonate (NaHCO3, AR) (Tianjin Chemical Reagent Sixth Factory Branch Factory, China). Ltd., China), sodium bicarbonate (NaHCO3, AR) (Tianjin Chemical Reagent Six Factory Branch, China), sodium chloride (NaCl, AR) (Tianjin Zhiyuan Chemical Reagent Co., Ltd., China), potassium chloride (KCl, AR) (Tianjin Komeo Chemical Reagent Co., Ltd., China), disodium hydrogen phosphate (Na2HPO4-12H2O, AR) (Tianjin Tianli Chemical Reagent Co., Ltd., China), potassium dihydrogen phosphate (KH2PO4, AR) (Tianjin, China) Dongli Tianda Chemical Reagent Factory, Dongli District, China), Penicillin-Streptomycin Mixed Solution (100X Double Antibody) (Beijing Regen Biotechnology Co., Ltd., China), Tetrazolium Blue Bromide MTT (AR) (Shanghai Yuanmu Biotechnology Co., Ltd., China), PBS Buffer (Shijiazhuang Dingchen Science and Technology Co., Ltd., China), dimethyl sulfoxide DMSO (AR) (Yueyang Xiangmao Pharmaceutical and Chemical Co. Ltd., China), trypsin-EDTA culture medium (Shanghai Yuanmu Biotechnology Co., Ltd., China).

2.2 Instruments and equipment

Waters2695 High Performance Liquid Chromatograph (Waters, United States), Mass Spectrometry using LCQ-DecaXP/Ad type (Thermo Electron, United States), AF-08 Miniature High Speed Pulverizer (Wenling City, China, Traditional Chinese Medicine Machinery Manufacturing Co., Ltd.), DHG-9055A Electric Drum Drying Oven (Shanghai Yihang Science and Technology Co., Ltd., China), BCD-206TASJX Intelligent Refrigerator (Qingdao Haier Co., Ltd., China), BSA223S-CW Electronic Analytical Balance (Sartorius, Germany), KQ32000V Ultrasonic Cleaning Machine (Kunshan City Ultrasonic Instrument Co., Ltd., China), ZQZY-C8V Triple Combined Full-Temperature Vibrating Incubator (Shanghai Chuyi Instrument Co., Ltd., China), PB Ltd., PB-10 pH meter (Sartorius, Germany), HiQ SiL C18V column (KYA TECH), ALLEGRA-64R Beckman tabletop centrifuge (Beckman, United States), CKX53 inverted microscope (OLYMPUS), 61M/SG-XSB-102B electron microscope (China Beijing Zhongxi-Yuanda Technology Co. Ltd.), DHP-9052 Constant Temperature Incubator (Shanghai Baidian Instrument Factory, China), YDS-50 Liquid Nitrogen Storage Tank (Changsha Mingjie Instrument Co., Ltd., China), DNM-9602G Enzyme Labeling Instrument (Beijing Plan New Technology Co., Ltd., China), Micropipettes (Gilson, France), ESCOAC2-4S1 Biological Safety Cabinet (ESCO, Singapore), INC153 CO2 Incubator (Memmer, Germany), SX-700 Autoclave (Tomy, Japan), Hematocrit Plate (Shanghai Precision, China), 20~200uL Pipette Gun (Thermo, United States), 96-well Cell Culture Plate (Corning).

3 Experimental methods

3.1 Methodological validation

Examination of exclusivity: A sample solution was prepared, and the elution solvent was used as a blank control solution. Following the determination of the standard curve, the sample was injected, and the peak area was measured to assess the method's exclusivity. Precision test: Five samples of isoliquiritigenin were accurately measured, injected, and the peak area was determined based on the standard curve to evaluate the method's precision. Repeatability test: Six sample solutions were prepared in parallel, injected, and the peak area was determined under high-performance liquid chromatography (HPLC) conditions to assess the method's repeatability. Stability test: The same sample solution was injected at 0, 2, 4, 8, 12, and 24 h, and the peak area was measured to evaluate stability over the 0-24 h period. Spiking recovery experiment: Six aliquots of each isoliquiritigenin sample solution were taken, and a control solution of isoliquiritigenin of known quality was added to each. The spiking recoveries were calculated, and the relative standard deviation (RSD) values were determined to assess the method's accuracy.

3.2 Isoliquiritigenin extraction by solid-state fermentation with *Aspergillus niger*

A total of 4 g of absolute dry weight licorice powder was weighed and placed in a 100 mL conical flask. Distilled water was added according to the material-liquid ratio, and the mixture was stirred

TABLE 1 Factors and levels.

Factor	cor Level		
	-1	0	1
A pH	3	4	5
BSolid-liquid ratio (g/mL)	1:1	1:2	1:3
CInoculation amount of A. niger (CFU/mL)	5.0 × 10 ⁵	1.0×10^{6}	2.0×10^{6}

thoroughly to create a solid fermentation medium, which was then sterilized. The effects of different pH values on the yield of isoliquiritigenin from licorice species were examined at pH levels of 3, 4, 5, 6, and 7. Additionally, to assess the impact of varying fermentation durations on isoliquiritigenin yield, incubation times of 2, 4, 6, and 8 days were employed. The influence of different material-liquid ratios on isoliquiritigenin yield was also investigated, with ratios of 1:1, 1:2, 1:3, 1:4, 1:5, and 1:6 being tested. Furthermore, the effect of varying inoculation amounts of $Aspergillus\ niger$ on isoliquiritigenin yield was analyzed, with inoculation amounts of $1\times10^5, 5\times10^5, 1\times10^6, 2\times10^6, 3\times10^6, 4\times10^6, 5\times10^6$ used. Following fermentation, 100 mL of a 75% ethanol solution was added to the medium at a 1:25 material-liquid ratio, mixed thoroughly, and extracted using ultrasonic waves in a water bath at 60 °C for 1.5 h. The extraction was performed while hot, and the resulting filtrate was collected and its volume measured.

3.3 Response surface experimental optimization

After the univariate study, the optimal conditions for each variable were determined, with pH, solid-liquid ratio, and *Aspergillus niger* inoculum as the independent variables, and the yield of isoliquiritigenin fractions as the dependent variable, while keeping the other factors consistent in accordance with the principles of the Response Surface Methodology (RSM) design (Table 1).

3.4 Traditional extraction methods of isoliquiritigenin

Ethanol reflux extraction method: Weigh 4 g of absolute dry licorice in a 250 mL round-bottom flask. Following a 1:25 material-to-liquid ratio, add 100 mL of a 75% ethanol solution, mix thoroughly, and perform reflux extraction at 60 $^{\circ}\text{C}$ in a water bath for 1.5 h. Filter the mixture while hot and collect the filtrate.

Ultrasonic extraction: Weigh 4 g of absolute dry licorice in a 250 mL round-bottom flask. Using the same 1:25 material-to-liquid ratio, add 100 mL of a 75% ethanol solution, mix well, and extract using ultrasonication at 60 $^{\circ}$ C in a water bath for 1.5 h. Filter the mixture while hot and collect the filtrate.

3.5 Preparation of isoliquiritigenin derivatives

isoliquiritigenin (200 mg, 0.78 mmol) was dissolved in 10 mL of tetrahydrofuran (THF). To the reaction solution, N_1N' -

carbonyldiimidazole (506 mg, 3.12 mmol) and two drops of triethylamine were added at room temperature, and the mixture was stirred for 4 h. Following this, a 30% aqueous dimethylamine solution (1.2 mL, 3.9 mmol) was introduced, and the reaction was monitored using thin-layer chromatography (TLC). Upon completion of the reaction, 40 mL of saturated aqueous ammonium chloride solution was added to quench the reaction. The aqueous phase was extracted multiple times with ethyl acetate (20 mL \times 3), and the organic phases were combined. Subsequently, the organic phase was washed with saturated saline (5 mL \times 2) and dried over anhydrous magnesium sulfate. After filtration and concentration, the yellow solid was obtained via column chromatography (200–300 mesh silica gel, PE/EA = 1: 2) (Figure 1A).

Isolation of isoliquiritigenin (200 mg, 0.78 mmol) was achieved by dissolving it in 10 mL of N,N'-dimethylformamide (DMF). A 1.0M solution of lithium bis(trimethylsilyl) sulfamate (LHMDS) in tetrahydrofuran (1.17 mL, 1.17 mmol) was added dropwise to the reaction mixture at -40 °C under nitrogen atmosphere, and the mixture was stirred for 15 min. Subsequently, methyl trifluoromethanesulfonate (0.18 mL, 1.56 mmol) was added dropwise to the reaction solution, with the reaction progress monitored using thin-layer chromatography (TLC). Upon completion, the reaction was quenched by the addition of 40 mL of saturated aqueous ammonium chloride solution. The aqueous phases were extracted several times with ethyl acetate (20 mL × 3), and the organic phases were combined. The combined organic phase was washed with saturated saline (5 mL × 2) and dried over anhydrous magnesium sulfate. The concentrated solution was then filtered and purified by column chromatography (200-300 mesh silica gel, PE/EA = 6:1), yielding a yellow solid (Figure 1B).

isoliquiritigenin (200 mg, 0.78 mmol) was dissolved in 10 mL of THF. A 1.0M lithium bis(trimethylsilyl) diamine (LHMDS) solution in tetrahydrofuran (1.17 mL, 1.17 mmol) was slowly added dropwise to the reaction mixture under nitrogen protection at 0 °C. The reaction was stirred for 15 min, after which acetic anhydride was added dropwise to the reaction mixture (0.15 mL, 1.56 mmol). The progress of the reaction was monitored by TLC, and upon completion, 40 mL of saturated aqueous ammonium chloride solution was added to quench the reaction. The aqueous phase was extracted with ethyl acetate (20 mL \times 3), and the organic phases were combined, washed with saturated saline (5 mL × 2), and dried over anhydrous magnesium sulfate. The mixture was then filtered and followed by separation on a column concentrated. (200-300 mesh silica gel, PE/EA = 1:1) to yield a yellow solid. The isoliquiritigenin derivative 3 was successfully prepared, and the synthetic process is depicted in (Figure 1C).

Finally, the derivative yields of the three substances were calculated. Calculation of derivative yields is shown in Equation 1.

Yield (%) =
$$\frac{\text{Actual yield}}{\text{Theoretical yield}} \times 100 \%$$
 (1)

The 1H-NMR spectrum and 13C-NMR spectrum were also determined by NMR using deuterated chloroform as solvent and TMS as internal standard.

3.6 Inhibitory effect of isoliquiritigenin and its derivatives on tumor cell proliferation detected by MTT assay

Cells were identified through observation and subsequently prepared as a cell suspension. The cell count was determined using a cell counting method, and the suspension was distributed into 96-well culture plates, with each well containing approximately 10^4 cells in 100 μ L. The cells in the 96-well plates were cultured overnight at 37 °C in a 5% CO₂ incubator. After 24 h, the culture solution was aspirated and discarded. The final concentrations of isoliquiritigenin and its derivatives in the 96-well plates were set at 6.25 μ mol/L, 12.5 μ mol/L, 25 μ mol/L, 50 μ mol/L, and 100 μ mol/L. The blank control group received an equal volume of the culture solution, which consisted of RPMI 1640 medium containing 10% fetal bovine serum. This group was cultured synchronously with the administration groups and the positive control group (37 °C, 5% CO₂ incubator) for 48 h. It underwent the same MTT staining procedure (200 µL MTT solution added to each well for 4 h) and subsequent DMSO dissolution steps. The absorbance value from this group was used as the baseline to correct for interference from medium components, reagents, and operational processes on the experimental results. Each treatment group consisted of six parallel wells, and the cells were incubated at 37 °C in a 5% CO2 incubator for an additional 48 h. Following this incubation, the supernatant was removed, and 200 µL of fresh culture solution was added to each well. Subsequently, 200 μL of MTT solution was added to each well, and incubation continued for 4 h. After this period, the supernatant was discarded, ensuring minimal liquid residue remained, and 100 µL of DMSO was added and mixed thoroughly by shaking for 10 min. The cell inhibition rate was calculated based on the absorbance values obtained using an enzyme labeling instrument at a wavelength of 490 nm, and is shown in Equation 2.

$$\label{eq:cellproliferation} \mbox{Cell proliferation rate \% = } \frac{\mbox{Mean OD of administered group - Mean OD of blank control group}}{\mbox{Mean OD value of blank control group}} \times 100\,\%$$

3.7 Establishment of mouse tumor models

Caki-1 cells were cultured and suspended in serum-free medium, adjusting the cell concentration to 2×10^6 cells/mL. Under aseptic conditions, the right anterior axillary subcutis and abdomen of the mice were sterilized using 75% ethanol, followed by the inoculation of 0.2 mL of the cell suspension per mouse, ensuring thorough mixing before each aspiration to establish a solid tumor model. Tumor volume was measured every 3 days. The mice were randomly divided into five groups, each containing ten mice, and received intraperitoneal (ip) administration post-inoculation. The experimental groups were administered ISL-bL at high, medium, and low doses of 50 mg/(kg·d), 25 mg/(kg·d), and 12.5 mg/(kg·d), respectively. The positive control group received IL-2 at a dose of 2.5×10^5 IU/(kg·d), while the model control group was given an equal volume of saline. Administration occurred once daily, with 0.2 mL per mouse, starting the day after inoculation. The animal room was well-ventilated, maintained at a temperature of 20 °C-22 °C and a humidity of 45%-50%. The environment was clean, quiet, and followed a natural circadian rhythm. The animals were fed a standard diet, equivalent to 3 g per mouse per day, with water provided continuously. Fresh drinking water was replaced daily, and bedding was changed every 2-3 days.

3.8 HE staining to observe the morphological changes of tumor tissues

Tumor tissues of appropriate size were fixed in a 4% paraformaldehyde solution, dehydrated, and embedded in clear paraffin. The samples were then sealed in neutral gel through a series of processes, including dewaxing, gradient ethanol dehydration, differentiation rinsing, and HE staining, after which they were placed under a microscope for observation. Finally, statistical analyses were performed using SPSS 18.0 and GraphPad Prism 6.01 software, with data from each group expressed as x \pm s. Sample comparisons were conducted using a one-way ANOVA test, and a P-value of less than 0.05 was considered statistically significant.

3.9 Determination of the effect of ISL-b on protein expression in Caki-1 cells by Western blot method

The effect of ISL-b on protein expression in Caki-1 cells was determined by Western blot. The protein samples were thawed at room temperature, processed and denatured. Then, gel preparation and electrophoresis were performed, followed by membrane transfer in sequence. The membranes were blocked overnight with 5% milk prepared in TBST, incubated with primary and secondary antibodies successively with washing steps in between. Finally, ECL color development was carried out in the dark, and imaging analysis was performed.

3.10 Intestinal bacteria group-metabolic mechanisms in the Caki-1 homozygous mouse model using 16SrRNA sequencing

On the first day following the completion of modeling, rat feces were aseptically collected into sterile EP tubes. For both the model group and the IL-2 positive control group, five mice were randomly selected, and their feces were pooled. Two samples were taken from each of the ISL groups categorized by low, medium, and high doses. Each sample consisted of feces from five randomly selected mice, from which 200 mg was extracted. The collected fresh feces were snap-frozen in liquid nitrogen for over 30 s and subsequently stored at –80 °C for future use. DNA extraction, amplification, and library construction were completed within 4 weeks to facilitate subsequent analysis.

The specific sequencing and analysis workflow is as follows: Illumina NovaSeq platform was used for paired-end sequencing (PE250). The sequencing depth was evaluated by rarefaction curves, and the sequencing depth was determined to be reasonable when the curves tended to be flat. Prior to alpha diversity analysis, normalization was performed using a minimum data volume threshold of 59,860. For data standardization, the minimum sample size normalization strategy was adopted, involving random sampling adjustment of effective sequences from all samples. For bioinformatics analysis, QIIME v1.9.1 was used for Tags quality control and alpha diversity index calculation; Uparse v7.0.1001 was used for OTU clustering with 97% identity. Additionally, FLASH v1.2.7 was used for sequence assembly, Vsearch for chimera filtering, and MUSCLE v3.8.31 for constructing

phylogenetic trees. The complete workflow was as follows: raw off-machine data were assembled into raw Tags by FLASH, then subjected to QIIME quality filtering to obtain clean Tags. After removing chimeras via Vsearch, effective sequences were obtained, which were subsequently used for OTU clustering, species annotation, and diversity analysis. The quality filtering criteria included truncating consecutive 3 or more bases with a quality score \leq 19 and removing Tags with a length less than 75% of the original sequence.

4 Results and analysis

4.1 Methodology establishment

4.1.1 Linear relationships

The HPLC conditions involved using a C18 column (4.6 \times 250 mm, $5 \mu m$) with UV detection at a wavelength of 350 nm. The mobile phase was composed of acetonitrile mixed with 0.5% aqueous acetic acid in a volume ratio of 32:68.5 (v/v). The injection volume was 10 μ L, with a flow rate of 1.0 mL/min, and the column temperature was maintained at 25 °C. The isoliquiritigenin standard was prepared in seven concentration gradients: 0.03125, 0.06250, 0.12500, 0.25000, 0.50000, 1.00000, and 2.00000 mg/mL, and analyzed using the aforementioned mobile phases. The peak area of isoliquiritigenin was measured by absorbance at 350 nm. Subsequently, a standard curve was constructed with the concentration of the isoliquiritigenin standard (X) plotted on the horizontal axis and the peak area (Y) on the vertical axis, leading to the derivation of the regression equation, with the resulting high-performance chromatogram presented in Figure 2A. Additionally, Figure 2B illustrates the standard curve for isoliquiritigenin, yielding the regression equation $y = 3 \times 10^7 x + 2 \times 10^6$ and a correlation coefficient of $R^2 = 0.9911$. A strong linear relationship between concentration and absorbance was observed within the range of 0-2.0 mg/mL.

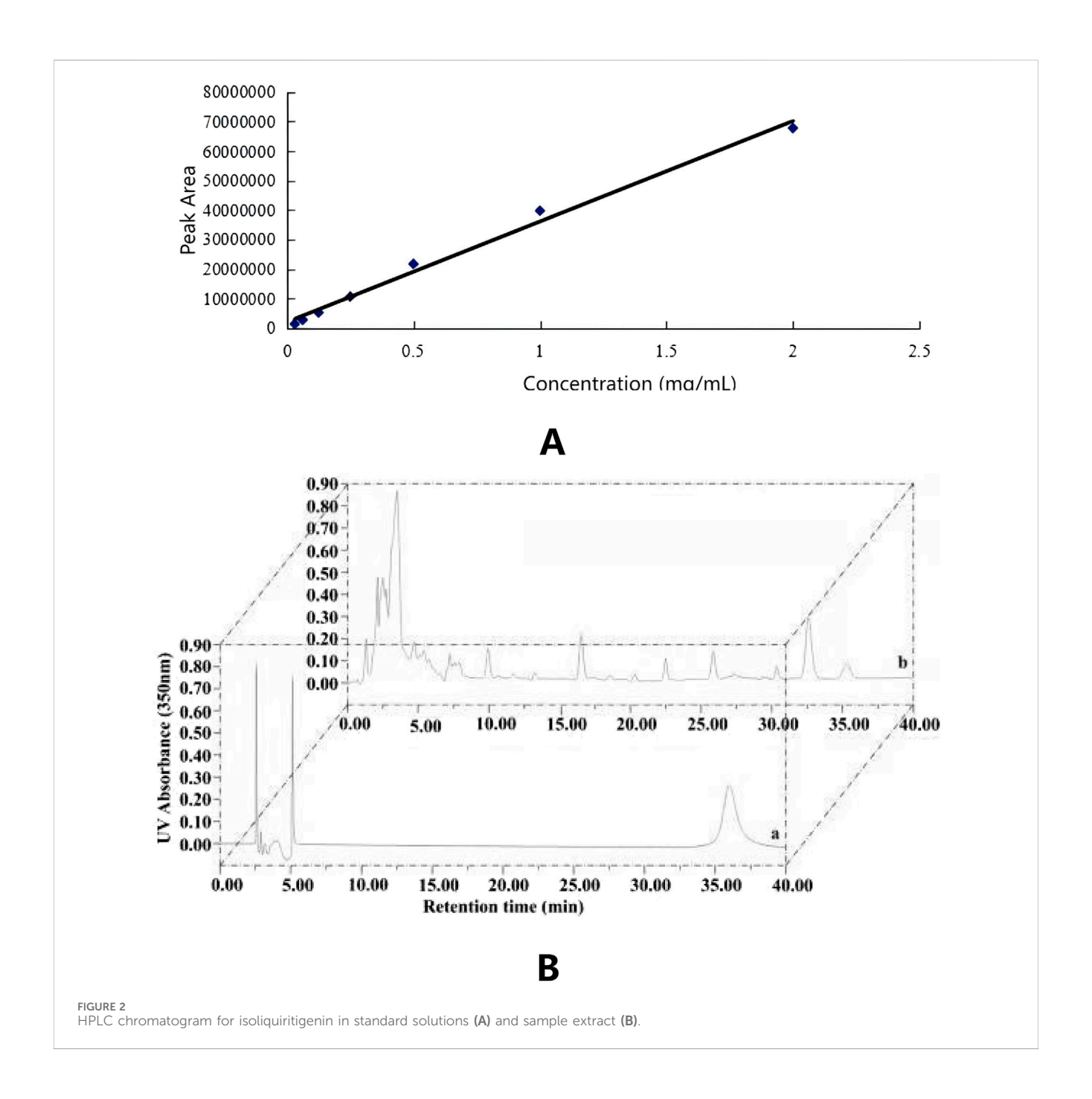
4.1.2 Methodological examination

Exclusivity test: The experimental results demonstrated that the blank test solution exhibited minimal absorbance under the chromatographic conditions, with no interference observed in the chromatographic analysis of the test material. This indicates that the established method possesses good exclusivity. Precision experiment: The RSD value is 0.42%, indicating that the precision of this method is satisfactory (Tables 2–5).

4.2 Optimization of isoliquiritigenin extraction by solid-state fermentation of *Aspergillus niger*

4.2.1 Effect of fermentation pH on the yield of isoliquiritigenin

The effect of fermentation pH on the yield of isoliquiritigenin from licorice is illustrated (Figure 3A). The yield of isoliquiritigenin was maximized at a pH of 4 and exhibited variability with differing pH levels. Specifically, the yield of isoliquiritigenin decreased as fermentation pH increased.



4.2.2 Effect of fermentation time on the yield of isoliquiritigenin

The effect of fermentation time on the yield of isoliquiritigenin was investigated. As illustrated in Figure 3B, the yield of isoliquiritigenin increased with an extended fermentation period, reaching its peak at 4 days.

4.2.3 Effect of fermentation solid-liquid ratio on the yield of isoliquiritigenin

The feed-liquid ratio significantly influences the yield of isoliquiritigenin extracted from licorice. The yield of isoliquiritigenin decreases with an increasing material-liquid ratio

(Figure 3C). The optimal yield of isoliquiritigenin was achieved at a material-liquid ratio of 1:2.

4.2.4 Effect of *Aspergillus niger* inoculum concentration on the extraction of isoliquiritigenin from glycyrrhiza uralensis fisch

The yield of isoliquiritigenin exhibited a linear increase with the rising concentration of Aspergillus niger, reaching its maximum yield at an inoculum concentration of 1.0×10^6 CFU/mL (Figure 3D). The mycelial biomass also peaked at the same inoculum concentration, indicating that the enzyme secretion achieved an optimal ratio with the substrate concentration

TABLE 2 Precision experiment results.

Content (mg/g)	Mean value (mg/g)	RSD (%)
0.413	0.416	0.420
0.415		
0.416		
0.417		
0.418		
0.415		

TABLE 3 Results of stability experiments.

Time (h)	Content (mg/g)	Mean value (mg/g)	RSD (%)
0	0.413	0.413	0.560
2	0.410		
4	0.414		
8	0.411		
12	0.416		
24	0.415		

TABLE 4 Repeatability experiment results.

Content (mg/g)	Mean value (mg/g)	RSD (%)
0.413	0.412	1.23
0.405		
0.414		
0.412		
0.419		
0.407		

(isoglycoside), thereby maximizing the efficiency of the catalytic reaction per unit time. Experimental data revealed that the yield was enhanced by approximately 65% when the inoculum concentration was raised from 1.0×10^5 to 1.0×10^6 , which aligns with the kinetic principle that the enzyme reaction rate increases linearly with enzyme concentration (Alves et al., 2018; Alarid-García et al., 2022).

4.3 Response surface method optimization

The interactions among these factors were investigated using Response Surface Methodology (RSM) to optimize fermentation pH, solid-liquid ratio, and the inoculum of *Aspergillus niger*. The experiments were randomized, and were designed to maximize the impact of unexplained variability on extraction efficiency. A total of 17 tests were conducted with 5 replications (specifically the 2nd, 7th, 8th, 12th, and 15th tests) to accurately estimate the pure sum of squares of errors (Table 6).

Based on the data presented, a multiple regression fitting analysis was conducted using Design Expert 8.0.7.1 software. The resulting quadratic equation for the yield of isoglycosides (Y) in relation to each factor variable is as follows: $Y\% = 1.49-0.016A + 0.054B + 0.20C - 0.095AB + 0.0025AC - 0.062BC - 0.049A^2 - 0.21B^2 - 0.33C^2$. The ANOVA results, indicate that the model is statistically significant with a p-value of less than 0.0001. Furthermore, the misfit term F-value of 33.51 suggests that the misfit is not significant (Table 7).

Based on the credibility analysis of the regression equation presented, the model's adjusted coefficient of determination is R^2 _adj = 0.9482, indicating that this model can explain 94.82% of the variation in the response variable. Additionally, the coefficient of determination is R^2 = 0.9773 and the predicted coefficient of determination is R^2 _pred = 0.8235, with a precision ratio of 18.461. This precision ratio suggests that the model is sufficiently precise, and the goodness of fit results are effective for predicting the yield of isoGlycyrrhiza uralensis Fisch under varying conditions for the yield of isoliquiritigenin. Furthermore, based on the comparison of F-values, it can be concluded that the order of significance under different conditions is as follows: Aspergillus niger inoculum > solid-liquid ratio > pH value (Table 8) (Figures 4A–F).

The optimal combination obtained from the response surface modeling calculation, along with the results analyzed and estimated using prediction software, yielded a pH of 3.694, a solid-liquid ratio of 1:2.155, an *Aspergillus niger* inoculum concentration of 1,466,745, and a yield of 1.525 mg/g. To enhance practical operational convenience, the extraction process parameters were adjusted to pH 3.694, a solid-liquid ratio of 1:2.155, and an *Aspergillus niger* inoculum concentration of 1,466,745 for three validation tests. The validation analysis produced a yield of 1.49 \pm 0.035 mg/g of isoliquiritigenin, demonstrating that these parameters effectively reflect the impact of screening factors on the yield of isoliquiritigenin.

TABLE 5 Experimental results of sample recovery.

Content (mg)	Amount of control added (mg)	Measured quantity (mg)	Recovery rate (%)	Average (%)	RSD (%)
1.02	1.01	1.99	98.03	98.20	0.52
1.00	1.02	1.98	98.02		
1.01	1.03	1.99	97.54		
1.06	1.00	2.03	98.54		
1.04	1.02	2.02	98.05		
1.05	1.01	2.04	99.02		

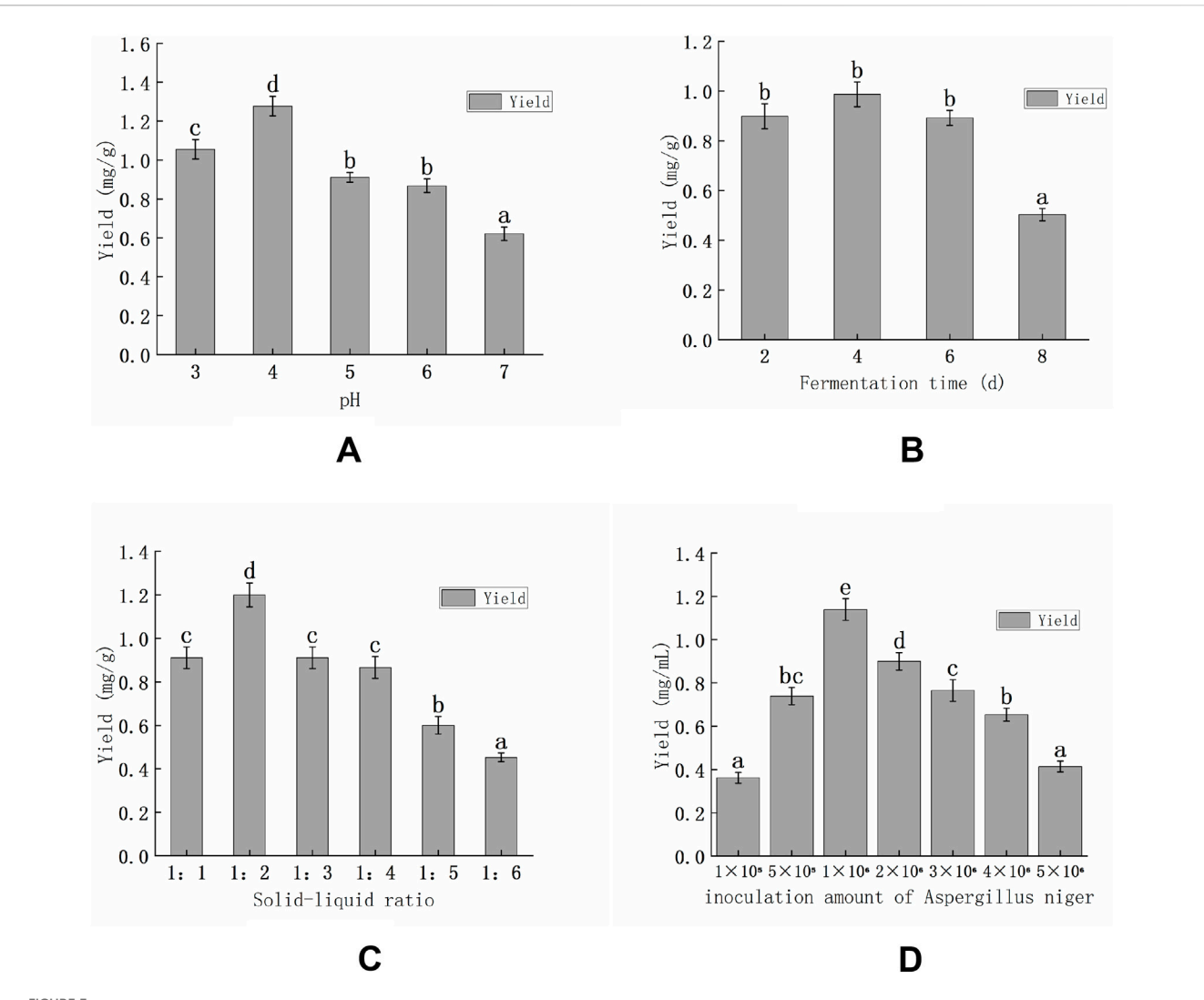


FIGURE 3
Effect of fermentation pH on isoliquiritigenin yield (A); Effect of fermentation time on isoliquiritigenin yield (B); Effect of fermentation solid-liquid ratio on isoliquiritigenin yield (C); D Effect of Aspergillus niger inoculum on isoliquiritigenin yield (D). (Note: Identical letters on the bar graph indicate a non-significant difference, while differing letters signify a significant difference between treatments) (P < 0.05). In the figure, a, b, c, d are symbols labeled after statistical analysis (such as multiple comparisons), used to characterize the difference conditions among different groups. Groups labeled with the same letter show no significant difference in the index, while groups labeled with different letters show significant differences.

4.4 Preparation of isoliquiritigenin derivatives and their structural characterization

4.4.1 Yield determination

Among them, the theoretical yield of ISL - a was 310 mg, the actual yield was 127 mg, and the yield was 40.9%; the theoretical yield of ISL - b was 221 mg, the actual yield was 175 mg, and the yield was 79.1%; the theoretical yield of ISL - c was 265 mg, the actual yield was 229 mg, and the yield was 86.4%. These data visualize the yield and profitability of each serial number (Table 9).

4.4.2 Identification of target compounds 4.4.2.1 Determination of chemical shifts of active hydrogens in isoglycosides

Isoliquiritigenin: ESI-MSm/z: 257.18 (M + H)+.1HNMR (400 MHz, DMSO-d6) δ 13.61 (s, 1H), 10.68 (s, 1H), 10.14

(s, 1H), 8.17 (d, J = 9.0 Hz, 1H), 7.76 (m, 4H), 6.84 (d, J = 8.6 Hz, 2H), 6.41 (dd, J = 8.9, 2.3 Hz, 1H), 6.28 (d, J = 2.3 Hz, 1H). 13CNMR (101 MHz, DMSO-d6) δ 191.43, 165.68, 164.85, 160.16, 144.17, 132.76, 131.13, 125.64, 117.30, 115.73, 112.88, 107.98, 102.47.

Isoliquiritigenin contains three hydroxyl groups situated at the 2- and 4-positions of the A-ring and at the 4'position of the B-ring. This paper focuses on structural modifications of isoliquiritigenin derivatives, specifically targeting the hydroxyl groups. Consequently, determining the chemical shifts of the active hydrogens in isoliquiritigenin is essential. Deuterated DMSO was employed as the solvent, and the final resolved data for isoliquiritigenin were obtained through analysis of the 1H-NMR, 13C-NMR, DEPT135, HSQC, and HMBC 1D and 2D NMR spectra (Supplementary Table 1A; Supplementary Table 1B; Supplementary Table 1C) (Figure 5).

TABLE 6 Box-Behnken experimental design.

Run	Factor A	Factor B	Factor C
	рН	Solid-liquid ratio (g/mL)	Inoculation amount of A. niger (CFU/mL)
1	5	3	1.25×10^{6}
2	4	2	1.25×10^{6}
3	4	1	5.00×10^{5}
4	3	1	1.25×10^{6}
5	4	3	5.00×10^{5}
6	5	2	2.00×10^{6}
7	4	2	1.25×10^{6}
8	4	2	1.25×10^{6}
9	3	2	2.00×10^{6}
10	5	2	5.00×10^{6}
11	4	3	2.00×10^{6}
12	4	2	1.25×10^{6}
13	3	3	1.25×10^{6}
14	4	1	2.00×10^6
15	4	2	1.25×10^{6}
16	5	1	1.25×10^{6}
17	3	2	5.00×10^{5}

TABLE 7 Analysis of variance (ANOVA) for regression equations.

Source	Sum of squares	Df	Mean square	F-value	<i>P</i> -value
Model	1.1100	9	0.1200	33.5100	<0.0001
A-pH	2.1120×10^{-3}	1	2.1120×10^{-3}	0.5700	0.4739
B-solid liquid ratio	0.0230	1	0.0230	6.2600	0.0408
C-inoculation amount of A. niger	0.3300	1	0.3300	88.9100	<0.0001
AB	0.0360	1	0.0360	9.7800	0.0167
AC	2.5000×10^{-5}	1	2.5000×10^{-5}	6.7760×10^{-3}	0.9367
ВС	0.0160	1	0.0160	4.2300	0.0786
A2	0.0100	1	0.0100	2.7800	0.1391
B2	0.1800	1	0.1800	50.0400	0.0002
C2	0.4600	1	0.4600	125.7100	<0.0001
Residual	0.0260	7	3.6900×10^{-3}		
Lack of Fit	0.0110	3	3.7080×10^{-3}	1.0100	0.4759
Pure Error	0.0150	4	3.6760×10^{-3}		
Cor Total	1.1400	16			

The chemical shift of the hydroxyl group at the C2 position is observed at 13.61 ppm, significantly higher than that of the hydroxyl groups at the C4 and C4 $^\prime$ positions. The peak shape indicates that the

hydrogen signal of C2-OH is sharper, whereas the signals from the generally active hydrogens, such as those from C4-OH and C4'-OH, are broader and less defined. This phenomenon can be attributed to

TABLE 8 The credibility analysis of the regression equations.

Index marka	Extraction efficiency of lignans
Std. Dev	0.0610
Mean	1.2100
C.V. %	5.0200
PRESS	0.2000
R-Squared	0.9773
AdjR-Squared	0.9482
PredR-Squared	0.8235
Adeq Precision	18.4610

the formation of an intramolecular hydrogen bond between the hydroxyl group at the C2 position and H-8, which results in an increased chemical shift and a sharper peak shape.

4.4.2.2 Activity of the hydroxyl group in isoliquiritigenin

Based on the experimental results presented in this paper, it is evident from the 1H-NMR spectra of compound 1 and compound 2 that the hydrogen signals corresponding to the hydroxyl groups at the C4 and C4' positions in isoglycyrrhetinin have disappeared within the chemical shift range of $\delta 10$ -11. This observation allows us to conclude that the reaction sites are located at the hydroxyl groups in the C4 and C4' positions, which exhibit similar reactivity without a specific sequential order. In contrast, the hydroxyl group at the C2 position demonstrates increased stability and is less likely to react with other chemical reagents. This stability can be attributed to the formation of intramolecular hydrogen bonding and the influence of steric hindrance, which impede the approach of substituent groups to this site.

4.4.2.3 Spectral analysis of isoliquiritigenin ISL-a

ISL-a: yellow solid 127 mg, 40.9% yield, melting point 124 °C–126 °C. ESI-MS, m/z: $C_{21}H_{23}N_2O_6$ [M + H]⁺, theoretical

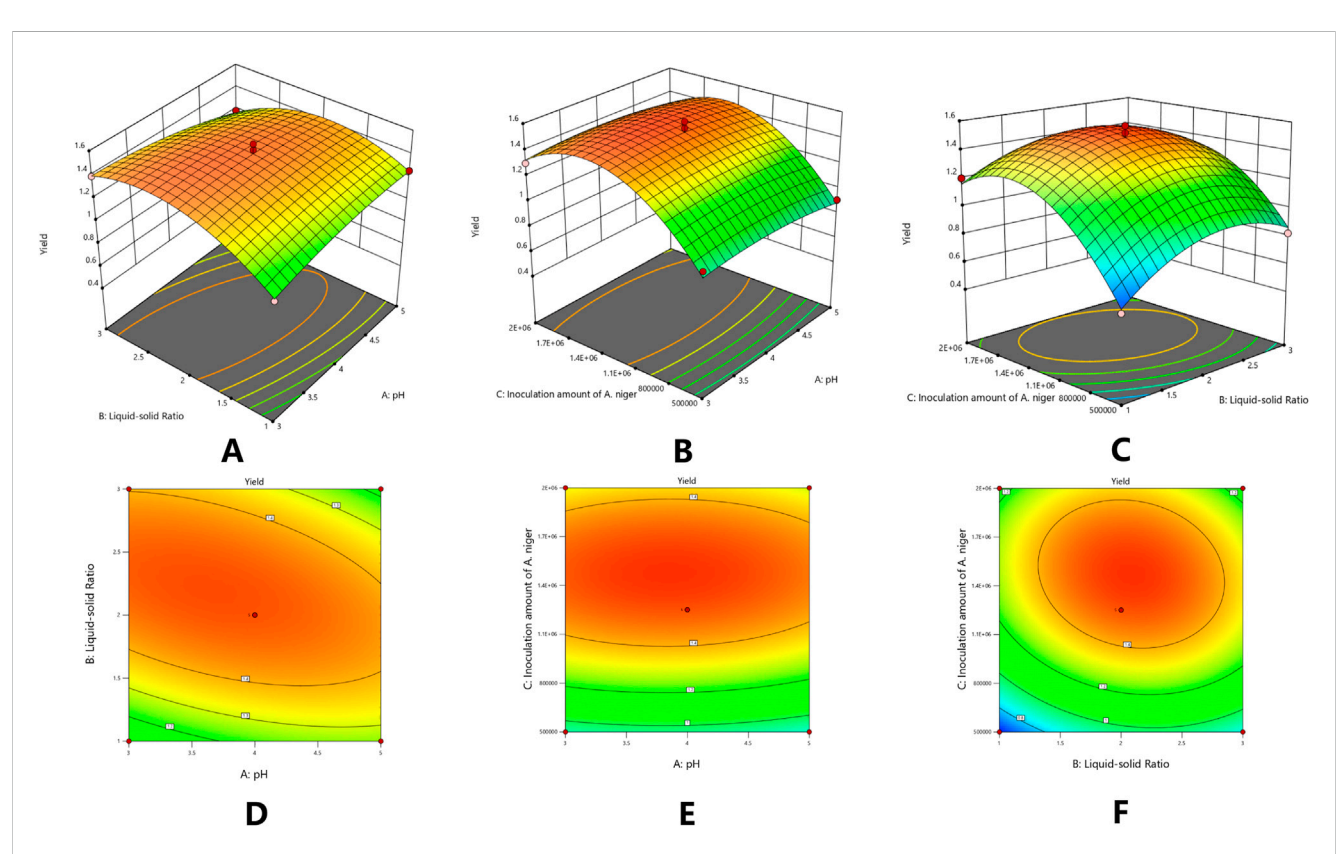


FIGURE 4
Response surface plots (3-D) of concentration of [BMIM] Br and extraction time on the yield of isoliquiritigenin (A); Response surface plots (3-D) of concentration of [BMIM] Br and solid-liquid ratio on the yield of isoliquiritigenin (B); Response surface plots (3-D) of extraction time and solid-liquid ratio on the yield of isoliquiritigenin (C-F).

TABLE 9 Yield of each derivative.

Serial number	Theoretical yield (mg)	Actual yield (mg)	Yield (%)
ISL-a	310	127	40.9
ISL-b	221	175	79.1
ISL-c	265	229	86.4

FIGURE 5 Schematic diagram of the chemical structure of isoliquiritigenin, with the numbering of carbon atoms (1-9) and 1'-6'.

value 399.17, measured value 399.42. ¹HNMR (400 MHz, CDCl3) δ 13.62 (s, 1H), 7.48 (d, J = 8.5 Hz, 2H), 7.14 (d, J = 8.5 Hz, 2H). 6.90 (d, J = 8.4 Hz, 1H), 6.72 (d, J = 2.2 Hz, 1H), 6.67 (dd, J = 8.4, 2.2 Hz, 1H), 6.08 (d, J = 3.6 Hz, 1H), 5.85 (d, J = 3.6 Hz, 1H), 2.31 (s, 3H), 2.29 (s, 3H), 2.09 (s, 6H). ISL-a 1 was identified as 4-[3-(4-dimethylaminocarbonyloxyphenyl)-acryloyl]-3-hydroxy-dimethylcarbamic acid phenyl ester (ISL-a).

4.4.2.4 isoliquiritigenin ISL-b spectral analysis

ISL-b: yellow solid 175 mg, yield 79.1%, melting point $131\sim132$ °C. ESI-MS, m/z: $C_{17}H_{17}O_4$ [M + H]⁺, theoretical value 285.11, measured value 285.20. ¹HNMR (400 MHz, DMSO-d6) δ 13.62 (s, 1H), 8.29 (d, J = 9.0 Hz, 1H), 7.90 (dd, J = 15.4, 8.8 Hz), 7.81 (d, J = 15.4, 8.8 Hz), 7.04 (d, J = 15.4 Hz, 2H), 6.57 (dd, J = 8.8 Hz, 2H), 3H), 7.81 (d, J = 15.4 Hz, 1H), 7.04 (d, J = 8.8 Hz, 2H), 6.57 (dd, J = 9.0, 2.5 Hz, 1H), 6.52 (d, J = 2.5 Hz, 1H), 3.85 (s, 3H), 3.83 (s, 3H). ISL-b was identified as (E)-1-(2-hydroxy4-methoxyphenyl)-3-(4-methoxyphenyl)-2-propen-1-one (ISL-b).

4.4.2.5 isoliquiritigenin ISL-c spectral analysis

ISL-c: yellow solid 229 mg, yield 86.4%, melting point 121~122 °C. ESI-MS, m/z: $C_{19}H_{17}O_6$ [M + H]⁺, theoretical value 341.10, measured value 341.13. HNMR (400 MHz, DMSO-d6) δ 13.61 (s, 1H), 8.17 (d, J = 9.0 Hz, 1H), 7.76 (dd, J = 5.2, 3.3 Hz 4H), 6.84 (d, J = 8.6 Hz, 2H), 6.41 (dd, J = 8.9, 2.3 Hz, 1H), 6.28 (d, J = 2.3 Hz, 1H), 2.26 (s, 6H). ISL-c was identified as (E)-1-(2-hydroxy4-acetoxyphenyl)-3-(4-acetoxyphenyl)-2-propen-1-one (ISL-c).

4.4.2.6 Structural confirmation conclusions

The structures of the isoliquiritigenin derivatives (ISL-a, ISLb, ISL-c) synthesized in this study were jointly confirmed through four independent sets of experiments: one-dimensional/twodimensional nuclear magnetic resonance (1D/2D NMR), mass spectrometry (MS), melting point determination, and HPLC purity validation. All characterizations were based on highpurity samples (≥98% purity) purified by HPLC. Method validation demonstrated precision (RSD = 0.42%), recovery (RSD = 0.52%, 98.20%), stability (RSD = 0.56%), and repeatability (RSD = 1.23%), effectively eliminating impurity interference and ensuring data reproducibility. Taking the most bioactive ISL-b (methoxy-modified derivative) as an example, the characteristic peaks in 1H-NMR include: methoxy proton peak (δ 3.85 s, 3H; δ 3.83 s, 3H), and trans double bond proton peak (δ 7.90 days, J = 15.4 Hz; δ 7.81 days, J =15.4 Hz) are clearly defined. HSQC coupling with ¹³C-NMR confirms methoxy attachment at C4 of ring A and C4' of ring B, while HMBC further establishes the core integrity of the "ring A - carbonyl - double bond - ring B" skeleton. ESI-MS measured its (M + H)+ peak at 285.20 Da (theoretical molecular weight deviation ≤0.25 Da). The melting point (131 °C–132 °C) overlaps with the literature range for similar chalcones, ruling out isomerism or substitution site errors. The characterization rationale for ISL-a and ISL-c aligns with ISL-b. ESI-MS (399.42 Da, 341.13 Da), melting points (124 °C-126 °C, 121 °C-122 °C), and 1D/2D NMR data all match theoretical structures. Furthermore, the C4/C4'-position methoxy modification in ISL-b aligns strongly with its optimal antitumor activity (Caki-1 cell IC50 = 15.304 µmol/L, tumor inhibition rate 56.3%), The p- π conjugation effect of the methoxy group enhances its binding affinity to the p65 protein in the NFκB pathway (Western blot analysis showed the most significant downregulation of p-p65 protein), providing structure-activity relationship evidence to support the rationality of the structural confirmation. In summary, the structural confirmation data for the three derivatives are comprehensive and logically rigorous, meeting the academic standards for structural characterization of new compounds.

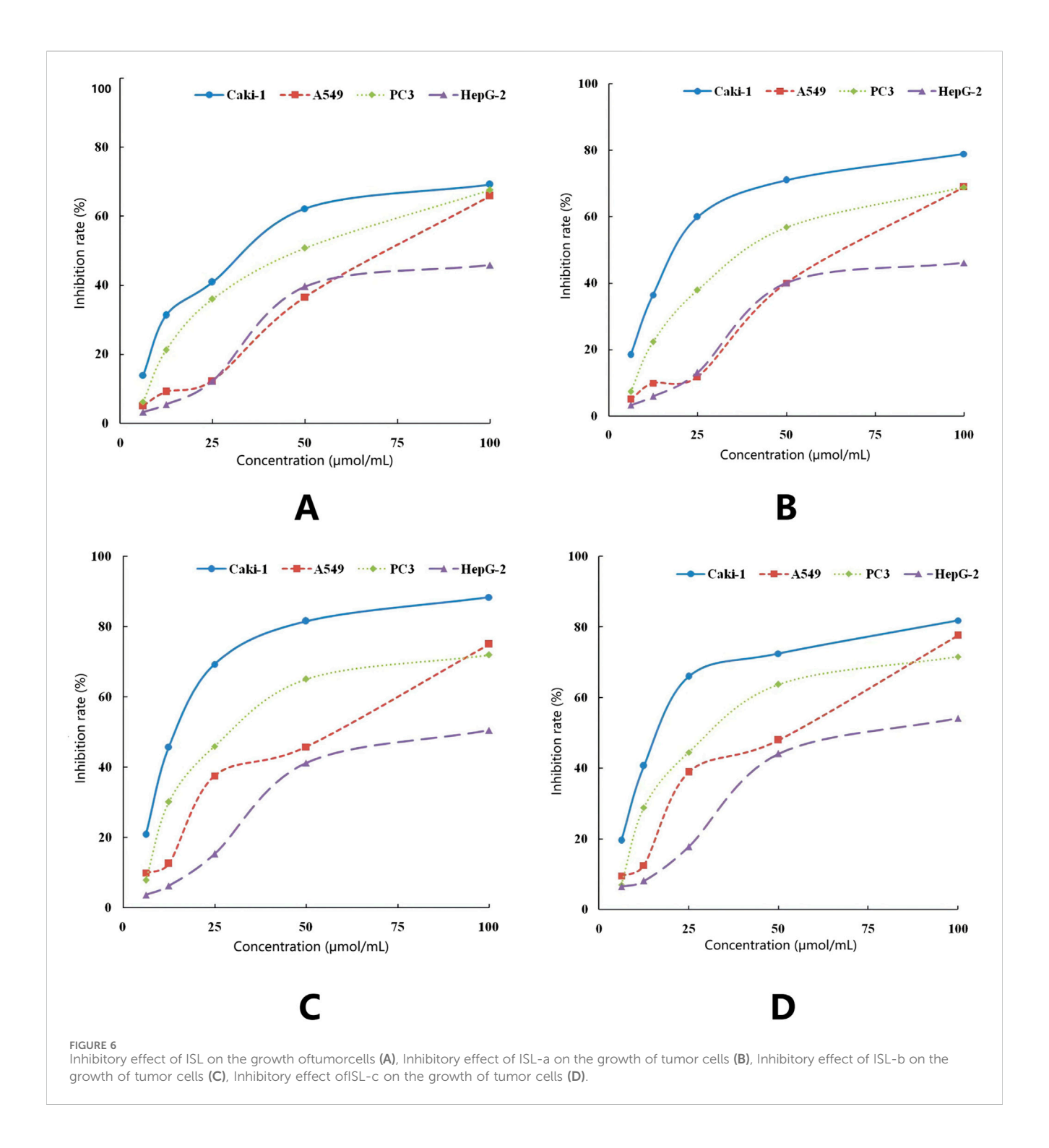
4.5 Inhibitory effect of isoliquiritigenin and its derivatives on tumor cell proliferation and cell morphology observation

4.5.1 Inhibition of tumor cell proliferation by isoglycosides and their derivatives

The cytotoxic effects of ISL and its derivatives on hepatocellular carcinoma HepG-2, lung cancer cell line A549, renal clear cell carcinoma Caki-1, and prostate cancer cell line PC-3 were assessed using the MTT assay. The IC50 values and inhibition rates of ISL and its three derivatives were calculated, following a 48-hour treatment period (Figures 6A–D). Notably, ISL and its derivatives exhibited superior inhibitory effects on renal clear cell carcinoma Caki-1, with IC50 values of 35.087 μ mol/L for ISL, 21.692 μ mol/L for ISL-a, 15.304 μ mol/L for ISL-b, and 18.611 μ mol/L for ISL-c. As illustrated in the graphs, the isoliquiritigenin derivative ISL-b demonstrated the most effective inhibition of Caki-1 cells in vivo (Table 10).

4.6 Morphological effects of isoliquiritigenin and derivatives on renal cancer cells (Caki-1)

Cell morphology was observed under an inverted microscope after treatment with ISL and its derivatives on Caki-1 cells at a concentration of 25 $\mu mol/L$ for 24 h. After 24 h of ISL treatment, most Caki-1 cells appeared to be in good condition, exhibiting adherent growth and well-defined edges; however, a few cells exhibited a rounded morphology. In the presence of the ISL-a compound, the number of rounded cells increased compared to the ISL-treated group, with non-adherent cells becoming evident and sparse growth observed, indicating that most cells were suspended in the culture medium. With the addition of the ISL-c



compound, the number of rounded and non-adherent cells further increased, while the growth rate of adherent cells significantly decreased. In the ISL-b treatment group, the morphological changes in Caki-1 cells were more pronounced compared to the ISL group; most cells became rounded, and the transparency and fullness of the cells decreased, with some cells appearing ruptured and a majority exhibiting signs of cell death. These results indicate that all three derivatives had a more pronounced inhibitory effect on Caki-1 cells than ISL, with ISL-b demonstrating the most significant efficacy (Figure 7).

4.7 Effects of isoglycosides and derivatives on Caki-1 hormonal mice

4.7.1 Effect of isoliquiritigenin and its derivatives on tumor volume changes in Caki-1 loaded mice

ISL-b was able to inhibit the growth of tumor volume in Caki-1 loaded mice, both of which were significantly different (P < 0.01 or P < 0.05) compared with the model control group, with the smallest tumor volume of Caki-1 in the ISL-b 50 mg/kg-d dose group (Table 11) (Figure 8A).

TABLE 10 Growth inhibition of tumor cells after 48 h of action of isoglycosides and their derivatives (x \pm s, n = 3).

Groups	IC50 (µmol/L)						
	Caki-1	A549	PC3	HepG-2			
ISL	35.087	70.604	47.643	96.782			
ISL-a	21.692	65.015	42.486	95.802			
ISL-b	15.304	46.405	32.762	85.548			
ISL-c	18.611	43.370	34.287	78.010			

4.7.2 Effect of isoglycosides and their derivatives on body weight changes in Caki-1 loaded mice

The model group of mice exhibited an increase in body weight over a duration of 13 days. In contrast, the IL-2 group experienced a

decrease in body weight due to the drug's toxic side effects, which resulted in reduced food intake. Conversely, the body weight of mice in the ISL-b dose groups remained stable. When compared to the model control group, no significant differences were observed in any of these groups (P > 0.05) (Table 12) (Figure 8B).

4.7.3 Effect of drugs on Caki-1 tumor tissue morphology

The histochemical results of hematoxylin and eosin (HE) staining of tumor tissue, it reveals that in the model group, cancer cells exhibit vigorous growth. The tumor cells are characterized by polygonal or spindle shapes, with pronounced nuclear polymorphism, displaying round, elliptical, or irregular shapes. The nuclear schizogenic image is evident, indicating a high nuclear-to-cytoplasmic ratio, while the cytoplasm appears light iridescent red. Tumor cells are distributed in patches and clusters, arranged closely together. In the IL-2 group and the ISL, ISL-b groups, an increase in apoptotic cells is observed,

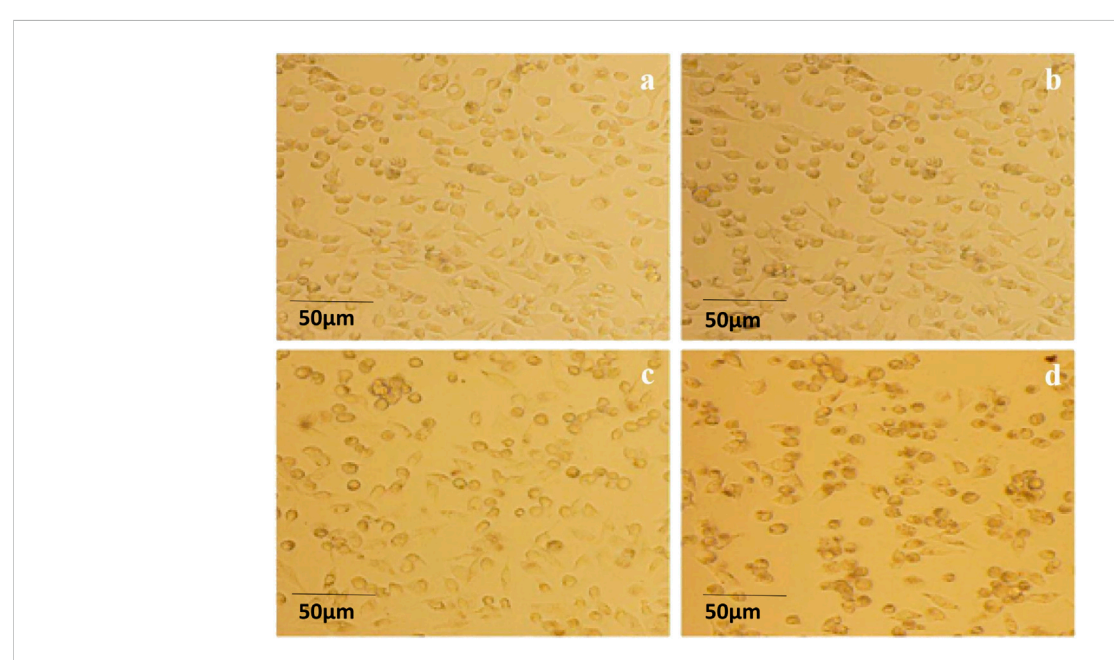


FIGURE 7
Morphological appearance of Caki-1 cells by optical microscope (200×) (a) ISL; (b) 25 μg/mLISL-a; (c) 25 μg/mL ISL-c; (d) 25 μg/mL ISL-b.

TABLE 11 Changes in tumor volume of Caki-1 tumor-bearing mice ($x \pm s$, n = 10, Unit: mm^2).

Day	Model	IL-2 2.5 × 10⁵IU/kg/d	ISL	ISL-b		
		2.3 × 10 10/kg/u	25 mg/kg-d	12.5 mg/kg-d	25 mg/kg-d	50 mg/kg-d
3	196.03 ± 11.02	220.23 ± 18.93*	193.42 ± 15.78	160.22 ± 12.04*	211.52 ± 16.04	218.44 ± 25.01*
5	214.9 ± 29.31	253.02 ± 21.27*	281.61 ± 18.33*	191.31 ± 18.13	265.65 ± 19.10*	269.61 ± 23.25*
7	385.27 ± 22.15	299.19 ± 25.82*	404.91 ± 25.16*	291.6 ± 26.07**	365.49 ± 23.16*	332.35 ± 28.79**
9	453.13 ± 24.07	355.36 ± 17.73**	555.60 ± 23.05**	401.22 ± 23.61*	413.39 ± 19.15*	346.37 ± 32.03**
11	526.28 ± 19.17	429.73 ± 22.16**	570.62 ± 26.13**	505.51 ± 20.15*	509.92 ± 22.47*	376.33 ± 31.02**
13	691.66 ± 30.36	532.78 ± 23.56**	620.70 ± 40.25**	631.98 ± 31.25**	572.14 ± 29.13**	458.53 ± 27.36**

Data are expressed as mean \pm standard deviation (x \pm s), n = 10.

Compared with the model group, *indicates P < 0.05 (significant difference), **indicates P < 0.01 (extremely significant difference).

Statistical method: One-way analysis of variance (ANOVA) with Bonferroni post-hoc test.

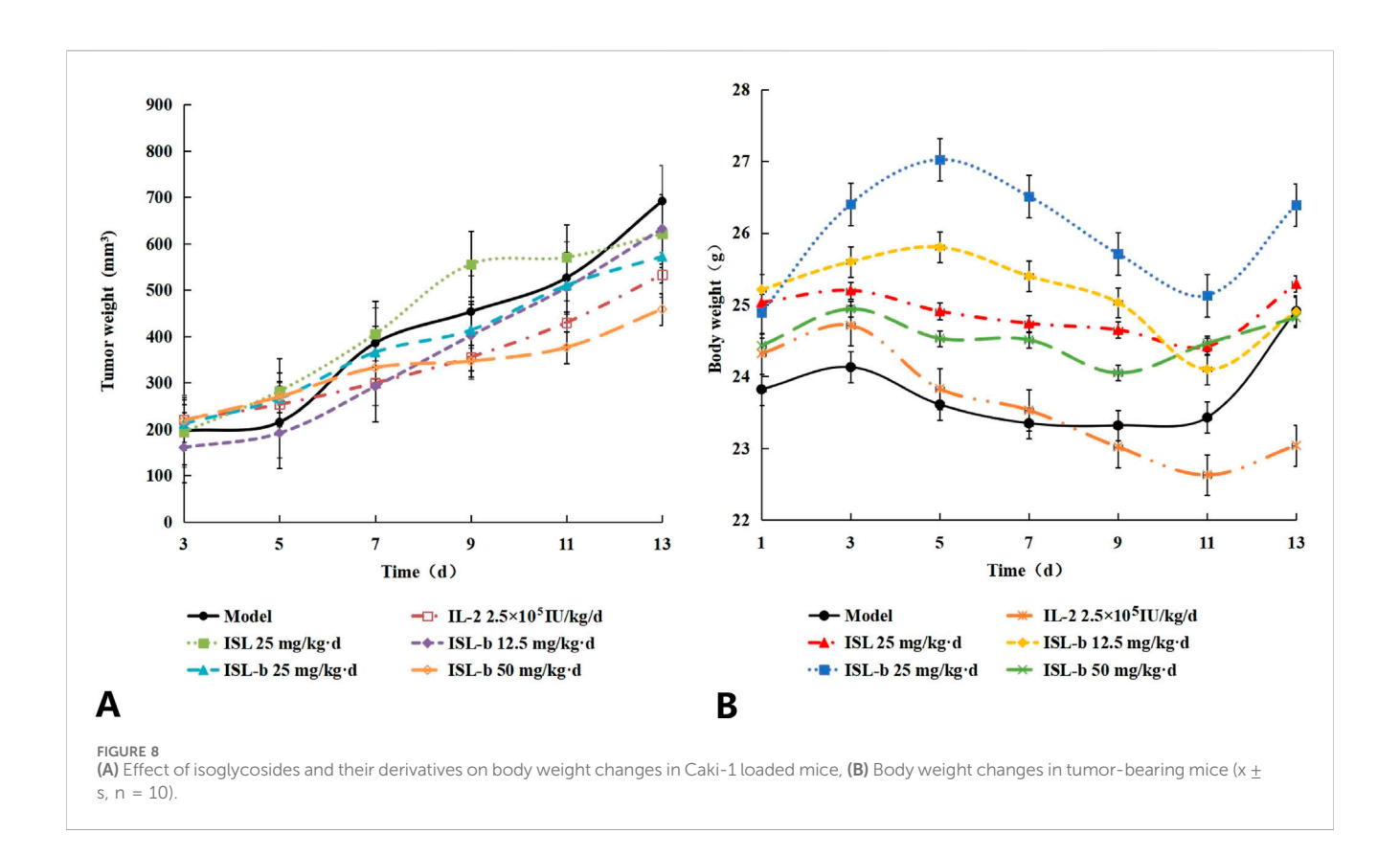


TABLE 12 Body weight changes in tumor-bearing mice (x \pm s, n = 10, Unit: g).

Day	Model	IL-2 2.5 × 10⁵IU/kg/d	ISL Stb 25 mg/kg-d 12.5 mg/kg-d 25 mg/kg-d 50 mg			
		2.5 x 10 10/kg/u		12.5 mg/kg-d	25 mg/kg-d	50 mg/kg-d
1	23.82 ± 0.95	24.32 ± 0.88	25.03 ± 1.12	25.21 ± 0.75	24.89 ± 0.48	24.43 ± 0.39
3	24.13 ± 1.02	24.71 ± 0.71	25.20 ± 1.03	25.60 ± 1.14	26.40 ± 0.74	24.94 ± 0.84
5	23.61 ± 0.87	23.83 ± 0.93	24.91 ± 0.89	25.80 ± 0.91	27.02 ± 0.82	24.53 ± 0.65
7	23.35 ± 0.76	23.53 ± 0.89	24.74 ± 0.77	25.40 ± 0.98	26.51 ± 0.68	24.51 ± 1.14
9	23.32 ± 0.85	23.02 ± 1.04	24.65 ± 0.94	25.03 ± 1.22	25.71 ± 0.53	24.05 ± 0.72
11	23.43 ± 1.01	22.63 ± 0.62	24.42 ± 0.86	24.10 ± 0.65	25.13 ± 0.71	24.46 ± 0.47
13	24.91 ± 0.91	23.04 ± 0.79	25.29 ± 0.92	24.90 ± 0.53	26.39 ± 1.17	24.82 ± 0.57

Data are expressed as mean \pm standard deviation (x \pm s), n = 10.

 $Compared \ with \ the \ model \ group, \ ^*indicates \ P < 0.05 \ (significant \ difference), \ ^**indicates \ P < 0.01 \ (extremely \ significant \ difference).$

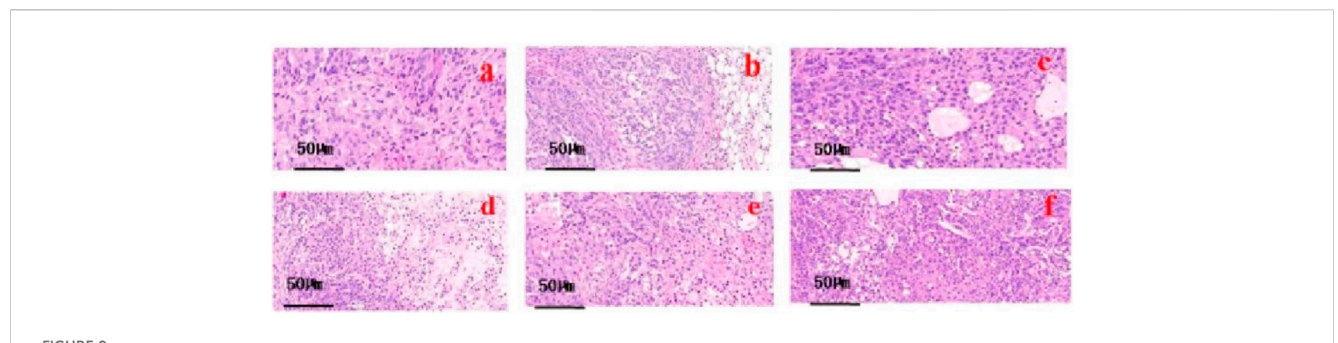
 $Statistical\ method:\ One-way\ analysis\ of\ variance\ (ANOVA)\ with\ Bonferroni\ post-hoc\ test.$

with these cells appearing separated from neighboring cells, and their nuclei are either condensed or even absent. In the ISL-b low and middle dose groups, tumor cells exhibit mild degenerative changes, with occasional large areas of necrosis. Conversely, tumor cells in the ISL-b high dose group display poorly defined contours, reduced density, and an increased necrotic area (Figure 9).

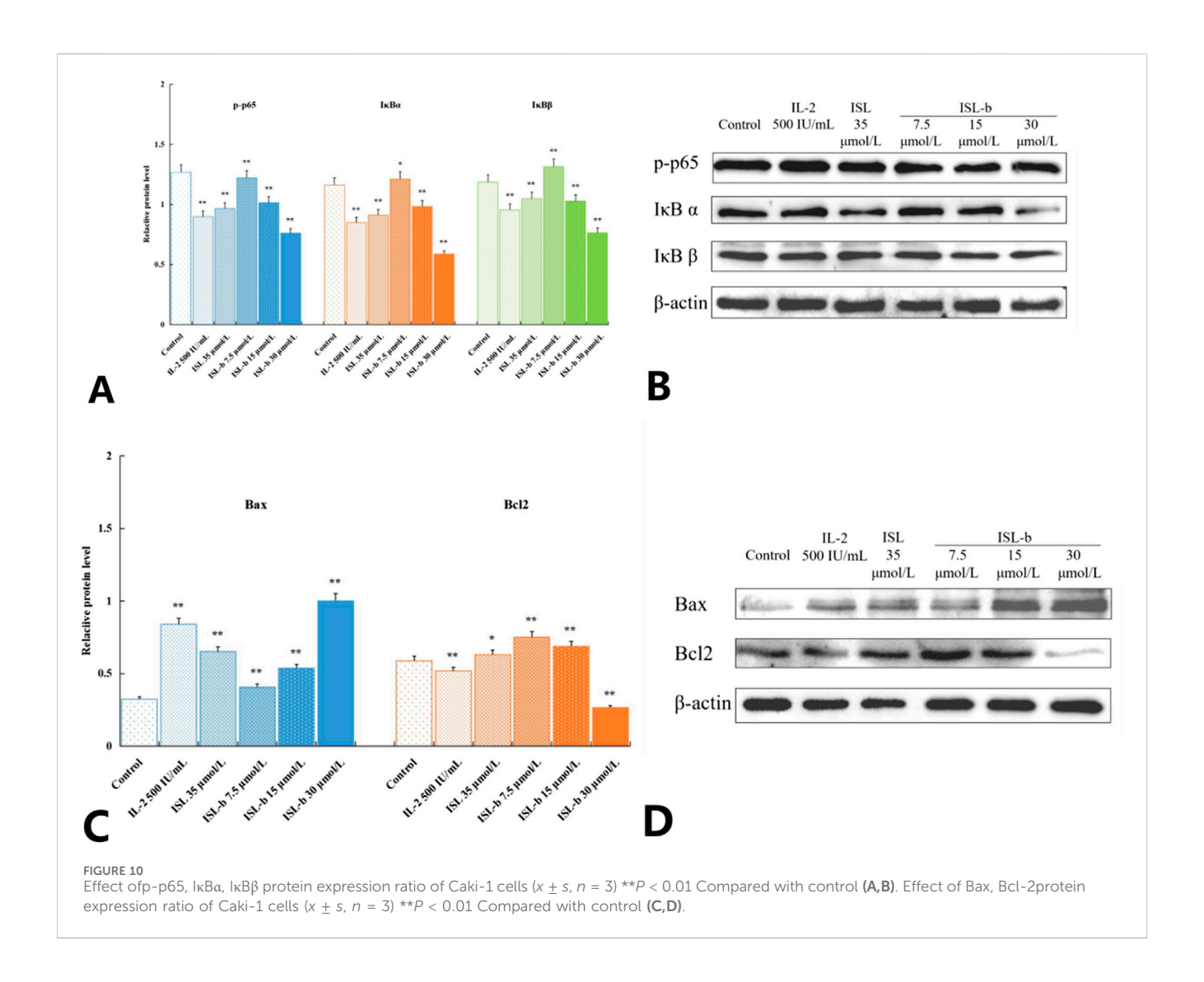
4.8 The effect of the drug on the expression of proteins related to the NF- κ B signaling pathway

Compared with the blank control group, after treatment with different concentrations of IL-2, ISL and ISL-b for 24 h, the expression levels of

p-p65, IkBa and IkBb proteins in Caki-1 cells decreased. Among them, after ISL-b treatment, the expression levels of p-p65, IkBa and IkBb proteins showed a negative correlation with concentration; the expression level of Bax, a pro-apoptotic protein downstream of the NF-kB signaling pathway, increased and showed a positive correlation with concentration; the expression of anti-apoptotic protein Bcl-2 decreased and showed a negative correlation with concentration. Statistical tests showed that there were statistically significant differences between the experimental groups and the blank control group (P < 0.05). The Bcl-2/Bax protein expression ratio was 1.8406 in the blank control group and 0.2654 in the high-dose ISL-b group (Figures 10A–D).



HE staining microscope of isoliquiritigenin and its derivatives on tumor tissue. (a) model group; (b) IL-2 group; (c) ISL group; (d) ISL-b high dose group; (e) ISL-b medium dose group; (f) ISL-b low dose group.



4.9 Differential analysis of intestinal flora in tumor-bearing mice

4.9.1 Alpha-diversity analysis

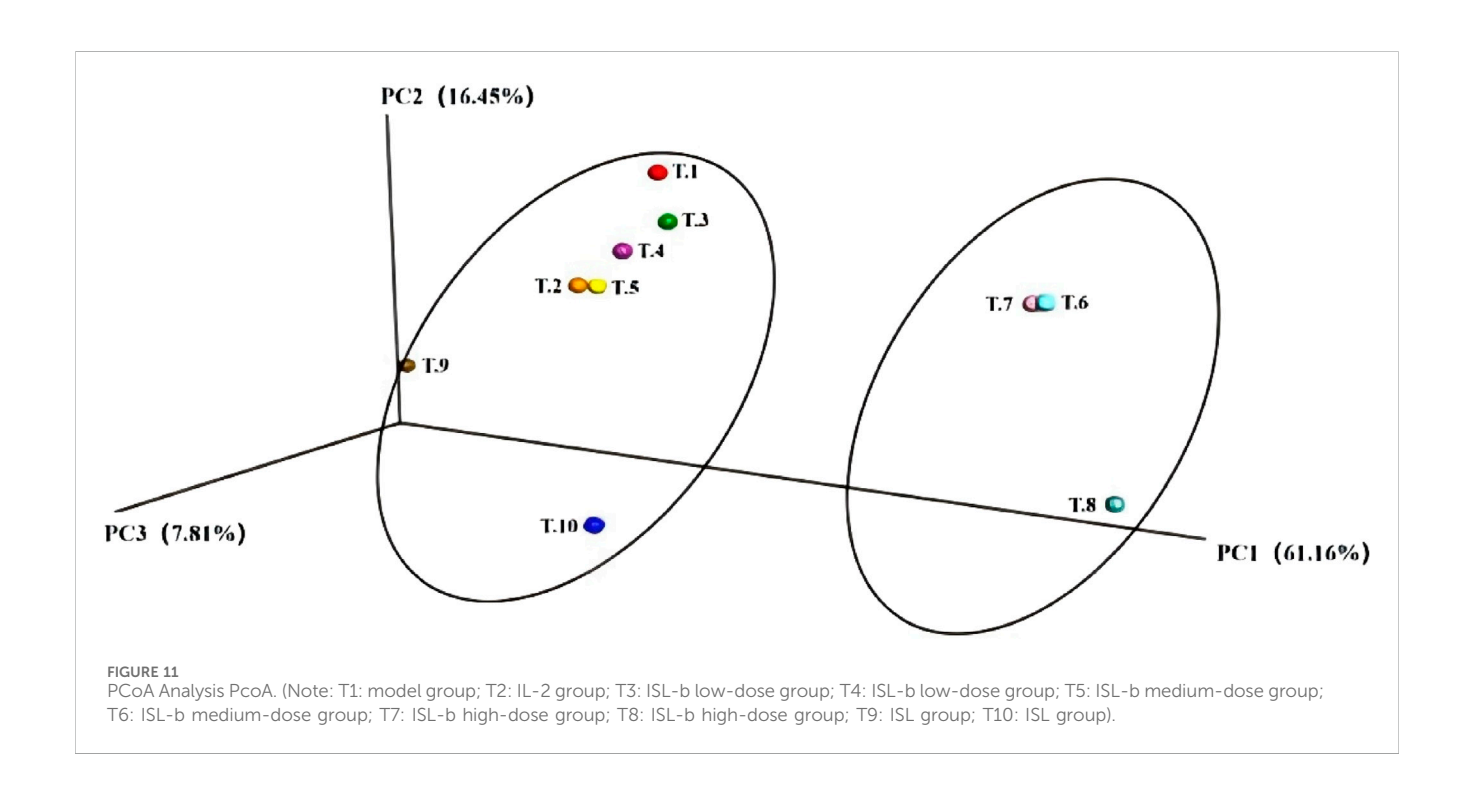
There was no significant difference in the number of observed species between the model group and the IL-2 drug group. However,

the model group exhibited higher Shannon diversity, greater community diversity, and a more even species distribution. When comparing the model group to the ISL-b high-dose group, the number of observed species was greater in the ISL-b high-dose group, indicating a higher species richness in this group. In contrast, the model group showed a lower number of observed species when

TABLE 13 Comparison of alpha diversity between the model group and each dosing group.

Sample name	Observed _species	Shannon	Simpson	chao1	ACE	Goods_coverage	Tree
Model group	497	5.038	0.930	542.493	542.354	0.999	56.845
IL-2	439	4.285	0.905	490.183	528.271	0.998	52.712
ISL-b low dose	387	4.373	0.908	418.544	427.056	0.999	45.379
ISL-b low dose	379	4.158	0.881	411.051	419.571	0.999	41.396
ISL-b Medium Dose	556	5.010	0.936	592.404	601.399	0.999	55.471
ISL-b medium dose	454	4.474	0.91	479.536	493.317	0.999	53.957
ISL-b High dose	640	4.974	0.922	698.579	721.151	0.998	85.293
ISL-b High dose	752	4.720	0.897	852.837	854.749	0.997	84.491
ISL	478	4.717	0.895	544.444	544.591	0.998	55.499
ISL	412	4.770	0.925	446.424	464.821	0.999	48.595

^{*}P < 0.05 Compared with model; **P < 0.01 Compared with model.



compared to the ISL-b medium and low-dose groups, suggesting a reduced species richness in these latter groups. Furthermore, the Chao1 index indicated that the total number of species present in the community samples was significantly greater in the ISL-b high-dose group (Table 13).

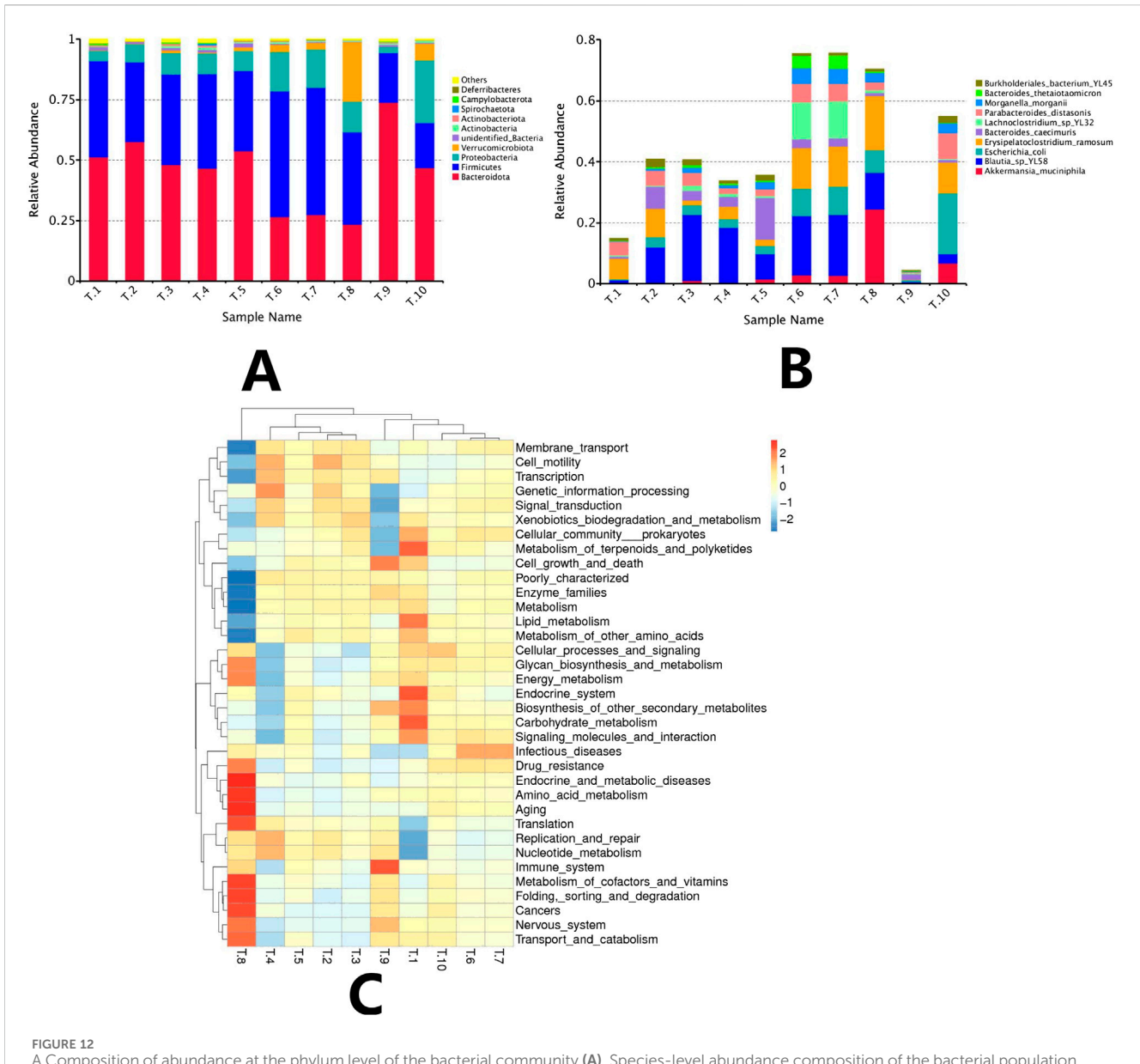
4.9.2 BetaDiversity analysis (BetaDiversity)

The model group, IL-2 group, ISL, and low-dose ISL-b group can be clustered together, while the medium and high-dose ISL-b groups form a separate cluster. This observation indicates significant differences in species composition within the intestinal feces. Furthermore, the high-dose ISL-b group is positioned further from the model group, suggesting that the species composition

between the high-dose ISL-b group and the model group exhibits greater differentiation (Figure 11).

4.9.3 Analysis of the structural composition of the intestinal flora in mice

Based on the results of species annotation, abundance histograms were plotted, and the top 10 microbial taxa at both the phylum and species levels were statistically analyzed in the model group and each drug group, respectively. The results indicated that the dominant phyla in each group were Bacteroidetes and Firmicutes. The model group exhibited the highest proportions of Bacteroidetes and Firmicutes, which together accounted for 90.9522%. In contrast, Verrucomicrobiota accounted for 0.1771% in the model group;



A Composition of abundance at the phylum level of the bacterial community (A). Species-level abundance composition of the bacterial population (B). (Note: T1: model group; T2: IL-2 group; T3: ISL-b low-dose group; T4: ISL-b low-dose group; T5: ISL-b medium-dose group; T6: ISL-b high-dose group; T7: ISL-b high-dose group; T8: ISL-b high-dose group; T9: ISL group). KEGG functional enrichment of differential genes in intestinal flora (C). (Note: T1: model group; T2: IL-2 group; T3: ISL-b low-dose group; T4: ISL-b low-dose group; T5: ISL-b medium-dose group; T6: ISL-b medium-dose group; T7: ISL-b high-dose group; T8: ISL-b high-dose group; T9: ISL group; T10: ISL group).

however, its abundance increased in the drug groups with rising drug concentrations. Notably, the ISL-b high-dose group demonstrated the highest percentage of Verrucomicrobiota at 24.49%. According to the species abundance histograms, there was a significant increase in the abundance of Akkermansia muciniphila and Blautia sp. YL58 at the species level, with A. muciniphila showing a corresponding increase in abundance with higher drug concentrations. In the high-dose ISL-b group, A. muciniphila accounted for 24.48%, which was 204 times greater than that observed in the model group (Figures 12A–C).

4.9.4 Analysis of the functional composition of the intestinal flora in each group of mice

KEGG functional enrichment analysis revealed that the differential genes of gut flora in the high-dose ISL-b drug group were primarily enriched in pathways related to cancers, translation, replication and repair, and nucleotide metabolism. In contrast, the model group exhibited enrichment in pathways associated with infectious diseases, drug resistance, endocrine and metabolic diseases, amino acid metabolism, and aging.

5 Discussion

China boasts extremely rich licorice resources with dual medicinal and ecological values, making the efficient development of its medicinal components (e.g., isoliquiritigenin, ISL) a critical research focus for both resource utilization and pharmaceutical innovation.

First, in optimizing ISL extraction from licorice, this study employed Aspergillus niger solid-state fermentation, achieving an extraction rate nearly 9-fold higher than traditional methods—a result that resolves a long-standing limitation of conventional techniques. As (Yu et al., 2020) documented, ISL in licorice exists in both glycogen-conjugated bound and free forms, but traditional methods only isolate free ISL, leading to underutilization of licorice resources. In contrast, our findings clarify that A. niger secretes βglucosidase during metabolism: this cellulase first disrupts licorice cell walls to release intracellular ISL (Pattanaik et al., 2022) and then hydrolyzes β-1,4 glycosidic bonds to convert bound ISL into free ISL (Cheng and DeYonker, 2022; Wu W. et al., 2022). While (Yang et al., 2022) previously reported that microbial enzymes can transform bound active components, our work advances this understanding by specifying the exact enzyme (β-glucosidase) and its target substrate (β-1,4 glycosidic bonds in licorice ISL)—filling a gap in the "microbe-enzyme-licorice ISL" interaction pathway that prior studies overlooked. Critically, few existing studies have quantified β-glucosidase's efficacy in licorice ISL extraction; our 9-fold yield increase provides concrete quantitative evidence, confirming the enzyme's role is not a general "efficiency boost" but a targeted solution to bound ISL underutilization.

Second, the chemical modification of ISL to synthesize ISL-b addresses key limitations of natural ISL and advances antitumor drug development. ISL, a hydroxychalcone with a C₁₅H₁₂O₄ molecular formula (Sun et al., 2021) and a flexible two-benzenering structure (Zhang et al., 2018), suffers from low oral absorption (Wang et al., 2018), photothermal/acidic instability, and nonspecific action-barriers to clinical application. Our strategy of introducing methoxyl groups (-OCH₃) at the C4 and C4' positions resolves these issues: the lone pair of electrons on methoxyl oxygen forms $p-\pi$ conjugation with the benzene ring, enhancing molecular electron cloud density and potentially strengthening binding affinity with the p65 protein in the NF-κB signaling pathway. Experimental results validate this modification: the ISL-b high-dose group exhibited a 56.3% tumor inhibition rate in Caki-1 tumor-bearing mice, with HE staining showing increased tumor cell apoptosis/necrosis, and routine blood tests/liver/kidney histology confirming no toxic side effects. Western blot analysis further supported the mechanism: ISL-b downregulated p-p65, ΙκΒα, and ΙκΒβ (NF-κΒ pathway proteins) in a concentrationdependent manner, upregulated the pro-apoptotic protein Bax, and downregulated the anti-apoptotic protein Bcl-2. However, critical gaps remain: derivative synthesis conditions were not systematically optimized, and exploration of other functional groups (e.g., ethoxy substitutions) is limited. Future work must address these to fully establish ISL's structure-activity relationship (SAR), a step essential for translating ISL derivatives into clinical use.

Third, ISL-b's regulation of intestinal flora reveals a dual antitumor mechanism, enriching understanding of natural products' antitumor action. A substantial body of research

confirms bidirectional interactions between tumors and intestinal flora: the tumor microenvironment shapes flora composition (Sánchez-Alcoholado et al., 2021; Wu N. et al., 2022), while flora metabolites regulate tumor proliferation and immune evasion (Zhang et al., 2021; Liu et al., 2022), forming a pathological interaction network (Dusek et al., 2020). Our results align with this framework: the ISL-b high-dose group showed higher intestinal flora biodiversity (Chao1 index) than the model group, with increased abundance of Micrococcus wartii (phylum level) and Akkermansia muciniphila (species level). A. muciniphila—a mucin-degrading anaerobe (Kim et al., 2021; Yan J. et al., 2021) that produces propionic acid (Shin et al., 2021; Segura Munoz et al., 2022) —interacts with host intestinal tissues via Gpr43 to modulate immunity (Giannoudaki et al., 2019; Stražar et al., 2021). However, our study did not link propionic acid to specific host immune factors, a gap that future research should fill to fully unravel the "flora-metabolite-immunity-tumor" regulatory axis.

Synthesizing these findings, this study makes three key contributions: it provides a scalable, high-efficiency ISL extraction process using *A. niger* fermentation, addressing licorice resource underutilization; it validates ISL-b as a safe, potent antitumor derivative targeting the NF-kB pathway, laying a foundation for clear cell renal cell carcinoma treatment; and it uncovers ISL-b's dual antitumor mechanism (direct pathway inhibition + indirect flora regulation), expanding insights into natural product pharmacology. These results not only advance basic research but also offer practical support for high-value licorice processing, aligning with the goal of sustainable medicinal resource development.

6 Conclusion

The process of extracting isoliquiritigenin from licorice was optimized using solid-state fermentation with Aspergillus niger and response surface methodology, resulting in a straightforward extraction process with a high yield. The results showed that the optimal extraction conditions were a pH of 3.7, a solid-liquid ratio of 1:2, an inoculation concentration of Aspergillus niger of 1.5×10^6 . After 4 days of fermentation, the yield of isoliquiritigenin was 1.53 mg/g. Isoliquiritigenin served as the substrate for structural modification, wherein the hydroxyl groups at both the C4 and C4' positions underwent the anticipated acylation or methylation reactions. ISL-b exhibited a growth inhibitory effect on Caki-1 cells derived from renal clear cell carcinoma, which intensified with increasing dosage. Furthermore, ISL-b effectively inhibited tumor growth in Caki-1 homozygous mice, reduced tumor volume, and preserved the body weight of the mice, indicating good drug safety. Variations in ISL-b concentration significantly influenced protein expression levels. Specifically, as ISL-b concentration increased, the expression levels of p-p65, IkBa, and $I\kappa B\beta$ proteins decreased, demonstrating a negative correlation. In contrast, the expression level of the pro-apoptotic protein Bax, which is downstream of the NF-κB signaling pathway, increased, showing a positive correlation with ISL-b concentration. Additionally, the expression level of the anti-apoptotic protein Bcl-2 exhibited a negative correlation with ISL-b concentration. Mice in the high-dose ISL-b group displayed significant alterations in intestinal flora, with notable upregulation of mucinophilic

Akkermansia muciniphila and Blautia sp. YL58. Furthermore, significant changes in the functional profiles of differential genes within the intestinal flora were observed in the high-dose ISL-b group.

Based on the results and limitations of this study, future research can be deepened in the following unexplored directions: First, in terms of the fermentation process, although core parameters such as pH and solid-liquid ratio have been determined, the synergistic effects of fermentation temperature (30 °C ± 2 °C) with other parameters on the activity of Aspergillus niger β-glucosidase and the accumulation of isoliquiritigenin (ISL) have not been systematically explored. Moreover, the current laboratory scale (100 mL Erlenmeyer flasks) does not involve issues such as uneven mass and heat transfer and solvent recovery in pilot-scale and industrial scale-up. In subsequent studies, it is necessary to supplement temperature gradient experiments and establish a 50-L scale fermentation system to verify the stability of the optimized process. Second, in the aspect of pharmacological research on ISL derivatives, it is known that ISL-b exerts antitumor effects by inhibiting the NF-kB signaling pathway, but it has not been verified whether ISL-b activates the ROS-mediated oxidative damage pathway (e.g., detecting ROS levels and caspase-3/ 9 expression in Caki-1 cells). Additionally, there is a lack of pharmacokinetic parameters (half-life, bioavailability) and longterm toxicity data (effects of 3-month repeated administration on hepatic and renal function). Relevant experiments need to be improved to support clinical translation. Third, in terms of derivative structure and intestinal flora mechanism, the structural characterization of ISL-a/-b/-c lacks high-resolution mass spectrometry (HRMS) data and complete 13C-NMR carbon skeleton assignment, and the structure-activity relationship (SAR) of other substituents (e.g., ethoxy groups) has not been explored. Meanwhile, regarding the mechanism by which ISL-b upregulates the abundance of Akkermansia muciniphila, the interaction between the metabolites of this bacterium (e.g., propionic acid) and host immune factors (e.g., IL-22) has not been linked. In subsequent studies, it is necessary to supplement structural confirmation experiments and explore the "flora-metabolite-immunity-tumor" regulatory network.

Data availability statement

The original contributions presented in the study are publicly available. This data can be found here: https://www.ncbi.nlm.nih.gov/sra/PRJNA1354458.

Ethics statement

Ethical approval was not required for the study involving animals in accordance with the local legislation and institutional requirements because This study only used standardized mouse cell lines purchased from commercial channels (specific institution name, such as ATCC) and did not involve live animal operations. According to the relevant regulations on ethical review, when using established commercial cell lines without live animal experiments, no additional ethical approval is required.

Author contributions

JH: Conceptualization, Data curation, Resources, Supervision, Writing – review and editing. QL: Visualization, Writing – original draft. ND: Formal Analysis, Investigation, Writing – original draft. YZ: Formal Analysis, Investigation, Methodology, Writing – original draft. YS: Investigation, Methodology, Visualization, Writing – original draft. YP: Investigation, Methodology, Visualization, Writing – original draft. XZ: Investigation, Writing – original draft. LY: Data curation, Supervision, Validation, Writing – review and editing.

Funding

The author(s) declare that financial support was received for the research and/or publication of this article. This research was supported by the Doctoral Entrepreneurship Fund Project of Mudanjiang Normal University (MNUB202316), the Cultivation Project of Joint Fund of Natural Science Foundation of Heilongjiang Province (PL 2024C023), the Basic Scientific Research Projects of Education Department of Heilongjiang (1451MSYYB005, 1453ZD026), the Research Project of Higher Education Teaching Reform in Heilongjiang Province (SJGY20220619), and the Postgraduate Scientific Technological Innovation Project of Mudanjiang Normal University (kjcx 2023-107mdjnu).

Acknowledgements

The authors express their gratitude to all those who supported the writing and submission of this article. Special thanks are extended to the Doctoral Entrepreneurship Fund Project of Mudanjiang Normal University (MNUB202316), the Cultivation Project of Joint Fund of Natural Science Foundation of Heilongjiang Province (PL 2024C023), the Basic Scientific Research Projects of Education Department of Heilongjiang Province (1451MSYYB005, 1453ZD026), the Research Project of Higher Education Teaching Reform in Heilongjiang Province (SJGY20220619), the Postgraduate Scientific and Technological Innovation Project of Mudanjiang Normal University (kjcx 2023-107mdjnu) for their financial support.

Conflict of interest

The authors declare that the research was conducted in the absence of any commercial or financial relationships that could be construed as a potential conflict of interest.

Generative Al statement

The author(s) declare that no Generative AI was used in the creation of this manuscript.

Any alternative text (alt text) provided alongside figures in this article has been generated by Frontiers with the support of artificial

intelligence and reasonable efforts have been made to ensure accuracy, including review by the authors wherever possible. If you identify any issues, please contact us.

reviewers. Any product that may be evaluated in this article, or claim that may be made by its manufacturer, is not guaranteed or endorsed by the publisher.

Publisher's note

All claims expressed in this article are solely those of the authors and do not necessarily represent those of their affiliated organizations, or those of the publisher, the editors and the

Supplementary material

The Supplementary Material for this article can be found online at: https://www.frontiersin.org/articles/10.3389/fphar.2025.1629167/full#supplementary-material

References

Alarid-García, C., Hernández-Calderón, O. M., Rios-Iribe, E. Y., González-Llanes, M. D., and Escamilla-Silva, E. M. (2022). Production of β -glucosidase by Aspergillus niger CDBB-H-175 on submerged fermentation. *Can. J. Chem. Eng.* 100, 1489–1501. doi:10.1002/cjce.24236

Ali, A., Park, Y., Lee, J., An, H.-J., Jin, J.-S., Lee, J.-H., et al. (2021). In vitro study of licorice on IL-1 β -induced chondrocytes and in silico approach for osteoarthritis. Pharmaceuticals 14, 1337. doi:10.3390/ph14121337

Alves, L. D. F., Meleiro, L. P., Silva, R. N., Westmann, C. A., and Guazzaroni, M.-E. (2018). Novel ethanol- and 5-hydroxymethyl furfural-stimulated β -glucosidase retrieved from a brazilian secondary atlantic forest soil metagenome. *Front. Microbiol.* 9, 2556. doi:10.3389/fmicb.2018.02556

Cai, S., Bi, Z., Bai, Y., Zhang, H., Zhai, D., Xiao, C., et al. (2020). Glycyrrhizic acid-induced differentiation repressed stemness in hepatocellular carcinoma by targeting c-jun N-terminal kinase 1. *Front. Oncol.* 9, 1431. doi:10.3389/fonc.2019.01431

Chen, W., Zhuang, J., Wang, P. P., Jiang, J., Lin, C., Zeng, P., et al. (2019). DNA methylation-based classification and identification of renal cell carcinoma prognosis-subgroups. *Cancer Cell Int.* 19, 185. doi:10.1186/s12935-019-0900-4

Chen, H.-Y., Chiang, Y.-F., Huang, J.-S., Huang, T.-C., Shih, Y.-H., Wang, K.-L., et al. (2021). Isoliquiritigenin reverses epithelial-mesenchymal transition through modulation of the TGF- β /smad signaling pathway in endometrial cancer. *Cancers* 13, 1236. doi:10.3390/cancers13061236

Cheng, Q., and DeYonker, N. J. (2022). A case study of the glycoside hydrolase enzyme mechanism using an automated QM-cluster model building toolkit. *Front. Chem.* 10, 854318. doi:10.3389/fchem.2022.854318

Das, A., Basak, S., Chakraborty, S., and Dhibar, M. (2022). Microwave: an ecologically innovative, green extraction technology. *Curr. Anal. Chem.* 18, 858–866. doi:10.2174/1573411018666220527095408

De Bruijn, V., Behr, C., Sperber, S., Walk, T., Ternes, P., Slopianka, M., et al. (2020). Antibiotic-induced changes in microbiome-related metabolites and bile acids in rat plasma. *Metabolites* 10, 242. doi:10.3390/metabo10060242

Dusek, O., Fajstova, A., Klimova, A., Svozilkova, P., Hrncir, T., Kverka, M., et al. (2020). Severity of experimental autoimmune uveitis is reduced by pretreatment with live probiotic escherichia coli nissle 1917. *Cells* 10, 23. doi:10.3390/cells10010023

Emaldi, M., and Nunes-Xavier, C. E. (2022). B7-H4 immune checkpoint protein affects viability and targeted therapy of renal cancer cells. *Cells* 11, 1448. doi:10.3390/cells11091448

Geng, J., Sui, Z., Dou, W., Miao, Y., Wang, T., Wei, X., et al. (2022). 16S rRNA gene sequencing reveals specific gut microbes common to medicinal insects. *Front. Microbiol.* 13, 892767. doi:10.3389/fmicb.2022.892767

Giannoudaki, E., Hernandez-Santana, Y. E., Mulfaul, K., Doyle, S. L., Hams, E., Fallon, P. G., et al. (2019). Interleukin-36 cytokines alter the intestinal microbiome and can protect against obesity and metabolic dysfunction. *Nat. Commun.* 10, 4003. doi:10. 1038/s41467-019-11944-w

Ji, J., Yu, J., Xu, W., Zheng, Y., Zhang, Y., and Sun, X. (2022a). Isolation and mechanistic characterization of a novel zearalenone-degrading enzyme. *Foods* 11, 2908. doi:10.3390/foods11182908

Ji, J., Zhang, S., Yuan, M., Zhang, M., Tang, L., Wang, P., et al. (2022b). Fermented rosa roxburghii tratt juice alleviates high-fat diet-induced hyperlipidemia in rats by modulating gut microbiota and metabolites. *Front. Pharmacol.* 13, 883629. doi:10.3389/fphar.2022.883629

Jiang, Q.-L., Lu, Y., Zhang, M.-J., Cui, Z.-Y., Pei, Z.-M., Li, W.-H., et al. (2022). Mucosal bacterial dysbiosis in patients with nodular lymphoid hyperplasia in the terminal ileum. *World J. Gastroenterol.* 28, 811–824. doi:10.3748/wjg.v28.i8.811

Kalantzakos, T. J., Sullivan, T. B., Gloria, T., Canes, D., Moinzadeh, A., and Rieger-Christ, K. M. (2021). MiRNA-424-5p suppresses proliferation, migration, and invasion of clear cell renal cell carcinoma and attenuates expression of O-GlcNAc-transferase. *Cancers* 13, 5160. doi:10.3390/cancers13205160

Kim, S., Shin, Y.-C., Kim, T.-Y., Kim, Y., Lee, Y.-S., Lee, S.-H., et al. (2021). Mucin degrader *akkermansia muciniphila* accelerates intestinal stem cell-mediated epithelial development. *Gut Microbes* 13, 1892441–20. doi:10.1080/19490976.2021.1892441

Kong, Y., Yang, B., Zhang, J., and Dong, C. (2022). Research progress on hydroxyl protection of iridoid glycosides. *Aust. J. Chem.* 75, 249–264. doi:10.1071/CH21260

Landberg, A., Fält, A., Montgomery, S., Sundqvist, P., and Fall, K. (2019). Overweight and obesity during adolescence increases the risk of renal cell carcinoma. *Int. J. Cancer* 145, 1232–1237. doi:10.1002/ijc.32147

Li, B., Li, M., Luo, Y., Li, R., Li, W., and Liu, Z. (2022a). Engineered 5-HT producing gut probiotic improves gastrointestinal motility and behavior disorder. *Front. Cell. Infect. Microbiol.* 12, 1013952. doi:10.3389/fcimb.2022.1013952

Li, M., Xiao, Y., Zhong, K., Wu, Y., and Gao, H. (2022b). Delving into the biotransformation characteristics and mechanism of steamed green tea fermented by aspergillus niger PW-2 based on metabolomic and proteomic approaches. *Foods* 11, 865. doi:10.3390/foods11060865

Liang, J., Li, B., Wen, L., Li, R., and Li, X. (2021). Thermal hydrolysis of wastewater sludge followed by fungal fermentation for organic recovery and hyphae fiber production. *Engineering* 7, 203–211. doi:10.1016/j.eng.2020.09.002

Liang, D., Feng, B., Li, N., Su, L., Wang, Z., Kong, F., et al. (2022). Preparation, characterization, and biological activity of cinnamomum cassia essential oil nano-emulsion. *Ultrason. Sonochem.* 86, 106009. doi:10.1016/j.ultsonch.2022.106009

Lima, L. G. R., Gonçalves, M. M. M., Couri, S., Melo, V. F., Sant'Ana, G. C. F., and Costa, A. C. A. D. (2019). Lipase production by aspergillus niger C by submerged fermentation. *Braz. Arch. Biol. Technol.* 62, e19180113. doi:10.1590/1678-4324-2010189112

Lin, C.-L., Hung, T.-W., Ying, T.-H., Lin, C.-J., Hsieh, Y.-H., and Chen, C.-M. (2020a). Praeruptorin B mitigates the metastatic ability of human renal carcinoma cells through targeting CTSC and CTSV expression. *Int. J. Mol. Sci.* 21, 2919. doi:10.3390/ijms21082919

Lin, P.-H., Chiang, Y.-F., Shieh, T.-M., Chen, H.-Y., Shih, C.-K., Wang, T.-H., et al. (2020b). Dietary compound isoliquiritigenin, an antioxidant from licorice, suppresses triple-negative breast tumor growth *via* apoptotic death program activation in cell and xenograft animal models. *Antioxidants* 9, 228. doi:10.3390/antiox9030228

Liu, Y., Hu, X., Zheng, W., Zhang, L., Gui, L., Liang, G., et al. (2022). Action mechanism of hypoglycemic principle 9-(R)-HODE isolated from cortex lycii based on a metabolomics approach. *Front. Pharmacol.* 13, 1011608. doi:10.3389/fphar.2022.

Lubna, Asaf, S., Jan, R., Khan, A. L., Bilal, S., Asif, S., et al. (2022). Unraveling the genome sequence of plant growth promoting aspergillus niger (CSR3) provides insight into the synthesis of secondary metabolites and its comparative genomics. *J. Fungi* 8, 107. doi:10.3390/jof8020107

Meng, Q., Ma, M., Zhang, W., Bi, Y., Cheng, P., Yu, X., et al. (2021). The gut microbiota during the progression of atherosclerosis in the perimenopausal period shows specific compositional changes and significant correlations with circulating lipid metabolites. *Gut Microbes* 13, 1–27. doi:10.1080/19490976.2021.1880220

Mittlmeier, L. M., Todica, A., Gildehaus, F.-J., Unterrainer, M., Beyer, L., Brendel, M., et al. (2022). 68Ga-EMP-100 PET/CT—a novel ligand for visualizing c-MET expression in metastatic renal cell carcinoma—first in-human biodistribution and imaging results. *Eur. J. Nucl. Med. Mol. Imaging* 49, 1711–1720. doi:10.1007/s00259-021-05596-6

Mohamad, O. A. A., Li, L., Ma, J.-B., Hatab, S., Xu, L., Guo, J.-W., et al. (2018). Evaluation of the antimicrobial activity of endophytic bacterial populations from Chinese traditional medicinal plant licorice and characterization of the bioactive secondary metabolites produced by bacillus atrophaeus against verticillium dahliae. *Front. Microbiol.* 9, 924. doi:10.3389/fmicb.2018.00924

Nasiri, L., Gavahian, M., Majzoobi, M., and Farahnaky, A. (2020). Rheological behavior of *Glycyrrhiza glabra* (Licorice) extract as a function of concentration and temperature: a critical reappraisal. *Foods* 9, 1872. doi:10.3390/foods9121872

- Park, J. S., Koo, K. C., Chung, D. Y., Kim, S. I., Kim, J., Oh, C. K., et al. (2020). Visceral adiposity as a significant predictor of sunitinib-induced dose-limiting toxicities and survival in patients with metastatic clear cell renal cell carcinoma. *Cancers* 12, 3602. doi:10.3390/cancers12123602
- Pattanaik, A., Sukla, L. B., Devi, N., Pradhan, N., and Pradhan, D. (2022). Tungsten dissolution from hutti goldmine overburden by aspergillus niger. Geomicrobiol. J. 39, 496–501. doi:10.1080/01490451.2022.2036878
- Qian, K., Fu, D., Jiang, B., Wang, Y., Tian, F., Song, L., et al. (2021). Mechanism of hedyotis diffusa in the treatment of cervical cancer. *Front. Pharmacol.* 12, 808144. doi:10.3389/fphar.2021.808144
- Sánchez-Alcoholado, L., Laborda-Illanes, A., Otero, A., Ordóñez, R., González-González, A., Plaza-Andrades, I., et al. (2021). Relationships of gut microbiota composition, short-chain fatty acids and polyamines with the pathological response to neoadjuvant radiochemotherapy in colorectal cancer patients. *Int. J. Mol. Sci.* 22, 9549. doi:10.3390/ijms22179549
- Scelo, G., Muller, D. C., Riboli, E., Johansson, M., Cross, A. J., Vineis, P., et al. (2018). KIM-1 as a blood-based marker for early detection of kidney cancer: a prospective nested case–control study. *Clin. Cancer Res.* 24, 5594–5601. doi:10.1158/1078-0432.CCR-18-1496
- Schäpe, P., Kwon, M., Baumann, B., Gutschmann, B., Jung, S., Lenz, S., et al. (2019). Updating genome annotation for the microbial cell factory *aspergillus niger* using gene co-expression networks. *Nucleic Acids Res.* 47, 559–569. doi:10.1093/nar/gky1183
- Segura Munoz, R. R., Mantz, S., Martínez, I., Li, F., Schmaltz, R. J., Pudlo, N. A., et al. (2022). Experimental evaluation of ecological principles to understand and modulate the outcome of bacterial strain competition in gut microbiomes. *ISME J.* 16, 1594–1604. doi:10.1038/s41396-022-01208-9
- Shi, W., Cao, X., Liu, Q., Zhu, Q., Liu, K., Deng, T., et al. (2022). Hybrid membrane-derived nanoparticles for isoliquiritin enhanced glioma therapy. *Pharmaceuticals* 15, 1059. doi:10.3390/ph15091059
- Shin, J., Noh, J.-R., Choe, D., Lee, N., Song, Y., Cho, S., et al. (2021). Ageing and rejuvenation models reveal changes in key microbial communities associated with healthy ageing. *Microbiome* 9, 240. doi:10.1186/s40168-021-01189-5
- Slivinski, C. T., Machado, A. V. L., Iulek, J., Ayub, R. A., and Almeida, M. M. D. (2011). Biochemical characterisation of a glucoamylase from aspergillus niger produced by solid-state fermentation. *Braz. Arch. Biol. Technol.* 54, 559–568. doi:10.1590/S1516-89132011000300018
- Stražar, M., Temba, G. S., Vlamakis, H., Kullaya, V. I., Lyamuya, F., Mmbaga, B. T., et al. (2021). Gut microbiome-mediated metabolism effects on immunity in rural and urban african populations. *Nat. Commun.* 12, 4845. doi:10.1038/s41467-021-25213-2
- Sun, L., Yang, Z., Zhang, J., and Wang, J. (2021). Isoliquiritigenin attenuates acute renal injury through suppressing oxidative stress, fibrosis and JAK2/STAT3 pathway in streptozotocin-induced diabetic rats. *Bioengineered* 12, 11188–11200. doi:10.1080/21655979.2021.2006978
- Susca, A., Proctor, R. H., Morelli, M., Haidukowski, M., Gallo, A., Logrieco, A. F., et al. (2016). Variation in fumonisin and ochratoxin production associated with differences in biosynthetic gene content in aspergillus niger and a. welwitschiae isolates from multiple crop and geographic origins. *Front. Microbiol.* 7, 1412. doi:10.3389/fmicb.2016.01412
- Swearson, S., Rataan, A. O., Eliason, S., Amendt, B. A., Zakharia, Y., Salem, A. K., et al. (2022). MicroRNA expression in clear cell renal cell carcinoma cell lines and tumor biopsies: potential therapeutic targets. *Int. J. Mol. Sci.* 23, 5604. doi:10.3390/iims23105604
- Tao, A., Feng, X., Sheng, Y., and Song, Z. (2022). Optimization of the artemisia polysaccharide fermentation process by aspergillus niger. *Front. Nutr.* 9, 842766. doi:10. 3389/fnut.2022.842766
- Ting, C.-T., and Chen, B.-S. (2022). Repurposing multiple-molecule drugs for COVID-19-associated acute respiratory distress syndrome and non-viral acute respiratory distress syndrome *via* a systems biology approach and a DNN-DTI model based on five drug design specifications. *Int. J. Mol. Sci.* 23, 3649. doi:10. 3390/ijms23073649
- Wang, Y., Zhou, P., Qin, S., Xu, D., Liu, Y., Fu, W., et al. (2018). The curcumin analogs 2-pyridyl cyclohexanone induce apoptosis via inhibition of the JAK2–STAT3 pathway in human esophageal squamous cell carcinoma cells. *Front. Pharmacol.* 9, 820. doi:10. 3389/fphar.2018.00820
- Wang, C., Li, P., Yan, Q., Chen, L., Li, T., Zhang, W., et al. (2019). Characterization of the pig gut microbiome and antibiotic resistome in industrialized feedlots in China. *Msystems* 4, e00206-19. doi:10.1128/msystems.00206-19
- Wang, L., Zhang, M., Wen, J., Xiang, Y., Duan, X., Yu, C., et al. (2021). Isoliquiritigenin alleviates semen strychni-induced neurotoxicity by restoring the metabolic pathway of neurotransmitters in rats. *Front. Pharmacol.* 12, 762290. doi:10.3389/fphar.2021.762290

- Wang, M., Wu, M., Liu, X., Shao, S., Huang, J., Liu, B., et al. (2022a). Pyroptosis remodeling tumor microenvironment to enhance pancreatic cancer immunotherapy driven by membrane anchoring photosensitizer. *Adv. Sci.* 9, 2202914. doi:10.1002/advs. 202202914
- Wang, Y., Ning, Y., He, T., Chen, Y., Han, W., Yang, Y., et al. (2022b). Explore the potential ingredients for detoxification of honey-fired licorice (ZGC) based on the metabolic profile by UPLC-Q-TOF-MS. Front. Chem. 10, 924685. doi:10.3389/fchem. 2022.924685
- Wong, W.-Y., Chan, B. D., Sham, T.-T., Lee, M. M. L., Chan, C.-O., Chau, C.-T., et al. (2022). Lactobacillus casei strain shirota ameliorates dextran sulfate sodium-induced colitis in mice by increasing taurine-conjugated bile acids and inhibiting NF-κB signaling via stabilization of IκBα. *Front. Nutr.* 9, 816836. doi:10.3389/fnut.2022.816836
- Wu, M., Liu, P., Wang, S., Zhong, C., and Zhao, X. (2021). Ultrasonic microwave-assisted micelle combined with fungal pretreatment of eucommia ulmoides leaves significantly improved the extraction efficiency of total flavonoids and gutta-percha. *Foods* 10, 2399. doi:10.3390/foods10102399
- Wu, N., Feng, Y.-Q., Lyu, N., Wang, D., Yu, W.-D., and Hu, Y.-F. (2022a). Fusobacterium nucleatum promotes colon cancer progression by changing the mucosal microbiota and colon transcriptome in a mouse model. *World J. Gastroenterol.* 28, 1981–1995. doi:10.3748/wjg.v28.i18.1981
- Wu, W., Zhang, X., Qu, J., Xu, R., Liu, N., Zhu, C., et al. (2022b). The effects of fermentation of qu on the digestibility and structure of waxy maize starch. *Front. Plant Sci.* 13, 984795. doi:10.3389/fpls.2022.984795
- Xie, J., Zheng, S., Zou, Y., Tang, Y., Tian, W., Wong, C.-W., et al. (2022). Turning up a new pattern: identification of cancer-associated fibroblast-related clusters in TNBC. *Front. Immunol.* 13, 1022147. doi:10.3389/fimmu.2022.1022147
- Xin, F., Wu, Y.-R., and He, J. (2014). Simultaneous fermentation of glucose and xylose to butanol by clostridium sp. Strain BOH3. *Appl. Environ. Microbiol.* 80, 4771–4778. doi:10.1128/AEM.00337-14
- Yan, J., Sheng, L., and Li, H. (2021a). Akkermansia muciniphila: is it the holy grail for ameliorating metabolic diseases? Gut Microbes 13, 1984104. doi:10.1080/19490976. 2021.1984104
- Yan, L., Yang, G., Cui, J., Miao, W., Wang, Y., Zhao, Y., et al. (2021b). Radiomics analysis of contrast-enhanced CT predicts survival in clear cell renal cell carcinoma. *Front. Oncol.* 11, 671420. doi:10.3389/fonc.2021.671420
- Yang, L., Yan, Y., Zhao, B., Xu, H., Su, X., and Dong, C. (2022). Study on the regulation of exogenous hormones on the absorption of elements and the accumulation of secondary metabolites in the medicinal plant artemisia argyi leaves. *Metabolites* 12, 984. doi:10.3390/metabol:2100984
- Yin, Y., Li, Y., Jiang, D., Zhang, X., Gao, W., and Liu, C. (2020). *De novo* biosynthesis of liquiritin in saccharomyces cerevisiae. *Acta Pharm. Sin. B* 10, 711–721. doi:10.1016/j. apsb.2019.07.005
- Yu, D., Liu, X., Zhang, G., Ming, Z., and Wang, T. (2018). Isoliquiritigenin inhibits cigarette smoke-induced COPD by attenuating inflammation and oxidative stress \emph{via} the regulation of the Nrf2 and NF- κ B signaling pathways. *Front. Pharmacol.* 9, 1001. doi:10.3389/fphar.2018.01001
- Yu, J., Zhang, D., Liang, Y., Zhang, Z., Guo, J., Chen, Y., et al. (2020). Licorice-yuanhua herbal pair induces ileum injuries through weakening epithelial and mucous barrier functions: saponins, flavonoids, and di-terpenes all involved. *Front. Pharmacol.* 11, 869. doi:10.3389/fphar.2020.00869
- Zhang, H., Wang, S., Zhang, X. X., Ji, W., Song, F., Zhao, Y., et al. (2016). The amyR-deletion strain of aspergillus niger CICC2462 is a suitable host strain to express secreted protein with a low background. *Microb. Cell Factories* 15, 68. doi:10.1186/s12934-016-0463-1
- Zhang, M., Wu, Y.-Q., Xie, L., Wu, J., Xu, K., Xiao, J., et al. (2018). Isoliquiritigenin protects against pancreatic injury and intestinal dysfunction after severe acute pancreatitis via Nrf2 signaling. Front. Pharmacol. 9, 936. doi:10.3389/fphar.2018.00936
- Zhang, S.-L., Mao, Y.-Q., Zhang, Z.-Y., Li, Z.-M., Kong, C.-Y., Chen, H.-L., et al. (2021). Pectin supplement significantly enhanced the anti-PD-1 efficacy in tumorbearing mice humanized with gut microbiota from patients with colorectal cancer. *Theranostics* 11, 4155–4170. doi:10.7150/thno.54476
- Zhang, M., Wang, X., Ayala, J., Liu, Y., An, J., Wang, D., et al. (2022). Combined urine metabolomics and 16S rDNA sequencing analyses reveals physiological mechanism underlying decline in natural mating behavior of captive giant pandas. *Front. Microbiol.* 13, 906737. doi:10.3389/fmicb.2022.906737
- Zhu, J., Huang, R., Yang, R., Xiao, Y., Yan, J., Zheng, C., et al. (2021). Licorice extract inhibits growth of non-small cell lung cancer by down-regulating CDK4-cyclin D1 complex and increasing CD8+ T cell infiltration. *Cancer Cell Int.* 21, 529. doi:10.1186/s12935-021-02223-0